



Article

A Multi-Model Ensemble Pattern Method to Estimate the Refractive Index Structure Parameter Profile and Integrated Astronomical Parameters in the Atmosphere

Hanjiu Zhang ^{1,2,3} , Liming Zhu ^{2,3,4} , Gang Sun ^{2,3,4,*}, Kun Zhang ^{2,3} , Ying Liu ^{1,2,3}, Xuebin Ma ^{2,3,4}, Haojia Zhang ^{2,3,4}, Qing Liu ^{2,3}, Shengcheng Cui ^{2,3,4} , Tao Luo ^{2,3,4} , Xuebin Li ^{2,3,4} and Ningquan Weng ^{1,2,3,4}

¹ School of Environmental Science and Optoelectronic Technology, University of Science and Technology of China, Hefei 230026, China; zhj999@mail.ustc.edu.cn (H.Z.)

² Advanced Laser Technology Laboratory of Anhui Province, Hefei 230037, China

³ Key Laboratory of Atmospheric Optics, Anhui Institute of Optics and Fine Mechanics, Hefei Institutes of Physical Science (HFIPS), Chinese Academy of Sciences, Hefei 230031, China

⁴ Science Island Branch of Graduate School, University of Science and Technology of China, Hefei 230026, China

* Correspondence: gsun@aiofm.ac.cn

Abstract: In this study, we devised a constraint method, called multi-model ensemble pattern (MEP), to estimate the refractive index structure parameter (C_n^2) profiles based on observational data and multiple existing models. We verified this approach against radiosonde data from field campaigns in China's eastern and northern coastal areas. Multi-dimensional statistical evaluations for the C_n^2 profiles and integrated astronomical parameters have proved MEP's relatively reliable performance in estimating optical turbulence in the atmosphere. The correlation coefficients of MEP and measurement overall C_n^2 in two areas are up to 0.65 and 0.76. A much higher correlation can be found for a single radiosonde profile. Meanwhile, the difference evaluation of integrated astronomical parameters also shows its relatively robust performance compared to a single model. The prowess of this reliable approach allows us to carry out regional investigation on optical turbulence features with routine meteorological data soon.

Keywords: optical turbulence; refractive index structure parameter; vertical profile; radiosonde; routine meteorological parameters; multi-model ensemble pattern; integrated astronomical parameters



Citation: Zhang, H.; Zhu, L.; Sun, G.; Zhang, K.; Liu, Y.; Ma, X.; Zhang, H.; Liu, Q.; Cui, S.; Luo, T.; et al. A Multi-Model Ensemble Pattern Method to Estimate the Refractive Index Structure Parameter Profile and Integrated Astronomical Parameters in the Atmosphere. *Remote Sens.* **2023**, *15*, 1584. <https://doi.org/10.3390/rs15061584>

Academic Editors: Xiaoming Wang, Yuriy Kuleshov, Suelynn Choy, Mayra I. Oyola-Merced and Haobo Li

Received: 15 February 2023

Revised: 5 March 2023

Accepted: 9 March 2023

Published: 14 March 2023



Copyright: © 2023 by the authors. Licensee MDPI, Basel, Switzerland. This article is an open access article distributed under the terms and conditions of the Creative Commons Attribution (CC BY) license (<https://creativecommons.org/licenses/by/4.0/>).

1. Introduction

Optical turbulence (OT), caused by atmospheric inhomogeneities and fluctuations, is one of the most critical factors that limit the transmission and performance of imaging systems [1]. Researchers involved in light propagation in the atmosphere, especially laser physicists and astronomers, have been concerned with this issue for decades [2–11]. A turbulent atmosphere impacts light wave propagation in various aspects, such as phase changes and intensity fluctuations. These distortions lead to significant blurring, scintillations, broadening, arrival angle fluctuations, and laser beam wander [1,2,8]. Hence, parameterization and characterization of OT are essential for designing and operating photoelectric systems.

Among all the parameters assessing the influence on optoelectronic systems from the turbulent atmosphere, the refractive index structure parameter (C_n^2) is commonly used to characterize the optical turbulence in the atmosphere. The past decades have witnessed researchers' efforts to measure, parameterize, and estimate C_n^2 . Up to now, different techniques (direct or indirect) using optical or non-optical principles have developed to obtain C_n^2 [12]. Among these techniques, a pair of micro-thermometers (MT) is the most common equipment used to obtain C_n^2 by invoking several hypotheses [1]. Utilizing a balloon-borne MT (in situ measurements), usually accompanied by measurements of routine meteorological parameters, is extensively employed for getting the C_n^2 profile in photoelectric

applications, for example, site testing [6,13,14] and astronomical observatories routine scheduling [3,15]. Other remote sensing methods and instruments, for example, Multi-Aperture Scintillation Sensor (MASS), Slope Detection And Ranging (Slodar) and Solar Differential Image Motion Monitor+ (S-Dimm+), are also of vital importance for the development of modeling and the refinement of empirical dependencies for astronomy [16–20].

Meanwhile, methods parameterizing and estimating C_n^2 profiles are established to meet the need of engineering practices. Empirical, physically-based, statistical, and data-driven learning methods to estimate C_n^2 were subsequently developed. Simple empirical methods, such as the submarine laser communication (SLC) model [21], are only involved in a single elevation parameter. Physically-based models referring to thermodynamics or dynamics factors exist in lots of literature. Owing to their abundant physical connotations, these models are competitive in characterizing OT in terms of its physical mechanism. Hufnagel developed the Hufnagel model based on meteorology and stellar scintillation data [22]. The Hufnagel-Valley5/7 (HV5/7) model [22,23] is one of the most popular forms related to wind velocity in the free atmosphere. Ruggiero and DeBenedictis proposed the Hmnsp99 outer scale model, referring to gradients of temperature and wind shear [24]. Dewan developed a similar turbulence outer scale method utilizing wind shear [25]. Thorpe investigated the relationship between potential temperature inversion and the Thorpe scale; Basu proposed a simple approach to estimate C_n^2 profiles with the coarse-resolution potential temperature profiles [21,26]. The Ellison scale was developed to quantify the scales of water body overturns. This theory was also used to calculate C_n^2 [27,28]. Recently, several modified models, such as the wind shear and potential temperature (WSPT) model [29] and wind shear and temperature gradient (WSTG) model [30], were also applied to estimate C_n^2 profiles under different experimental environments. Other methods were developed in a statistical view, for example, statistical models devised by Vanzandt [31] and Trinquet [32]. Along with the development of computer science, deep learning tools have shown their advantage in handling high-dimensional and nonlinear issues. Researchers also applied this useful tool in estimating C_n^2 [33–35].

However, no one of the existing estimating approaches are superior to any of the others, to the best of our knowledge. Each existing approach has its own merits and limitations [21]. The universality and robustness of most existing approaches and models should be improved. However, the turbulent atmosphere with random, nonlinear, and infinite-element features makes it difficult to completely specify the precise mathematical expression of C_n^2 from the routine macroscopic meteorological parameters—for now, at least. The existing physical-based approaches were established on several hypotheses and statistical evidence, more or less. Here, we propose a multi-model ensemble pattern (MEP) method to estimate C_n^2 based on several existing physically-based methods. The purpose of this study is to take advantage of different existing approaches. The proposed model performance is not always the best. However, it can ensure that the C_n^2 and integrated astronomical parameters estimated by the MEP are competitive compared to the best of the existing models if it is not.

This paper is organized as follows: Section 2 describes the experimental site, instruments, and radiosonde data. Section 3 presents the theory of several existing approaches to estimate C_n^2 that we adopted and the proposed MEP method. Section 4.1 depicts the results of C_n^2 using different models. Section 4.2 exhibits the evaluation of different models in calculating integrated astronomical parameters. The summary and conclusions are given in Section 5.

2. Experimental Principles and Scientific Data

2.1. Experimental Principles

According to the Gladstone law [12,36] and neglecting the water vapor concentration contribution, the refractive index structure parameter C_n^2 ($\text{m}^{-2/3}$) can be computed via

pressure P (hPa), absolute temperature T (K), and temperature structure parameter C_T^2 ($\text{K}^2 \text{m}^{-2/3}$) as follows:

$$C_n^2 = \left(79 \times 10^{-6} \frac{P}{T^2} \right)^2 C_T^2. \quad (1)$$

C_T^2 can be calculated by the temperature structure function D_T^2 based on the Kolmogorov–Obukhov turbulence assumption [1]. D_T^2 is defined as:

$$D_T(r) = \langle [T(\vec{x}) - T(\vec{x} + \vec{r})]^2 \rangle = C_T^2 r^{2/3} (l_0 \ll r \ll L_0), \quad (2)$$

where triangle brackets denote an ensemble average; \vec{x} and $\vec{x} + \vec{r}$ are the positions of the temperature probes; l_0 and L_0 represent the inner and outer scales, respectively; and r represents the distance of two probes that should be in the inertial sub-region. Radiosonde balloons equipped with micro-thermometers (MT) and routine meteorological sensors are used worldwide to obtain optical turbulence and meteorology parameters profiles.

In our case, the temperature probes (red rectangular boxes) used are shown in Figure 1b. The two platinum probes were isolated 1 m ($r = 1$ m) horizontally. T and P data necessary for calculating C_n^2 were measured by onboard temperature and pressure sensors. A Global Positioning System (GPS) was used to obtain the position information, and wind velocity was calculated from GPS data with a precision of 0.3 m/s. The Anhui Institute of Optics and Fine Mechanics (AIOFM) designed the whole system. The instruments' performance was summarized in Ref. [37]. The platinum wire probe resistance was 10Ω with $10 \mu\text{m}$ diameter. The minimum detectable value of C_T^2 was $4.0 \times 10^{-6} \text{ K}^2 \text{m}^{-2/3}$. The sampling frequency of the processor was up to 100 Hz, and the data were averaged with a time interval of 1 s. The precision of the temperature and pressure sensors were 0.2 K and 1.5 hPa. The balloons ascend with a vertical velocity of approximately 5 m/s. The data were re-processed with a space interval of 10 m.

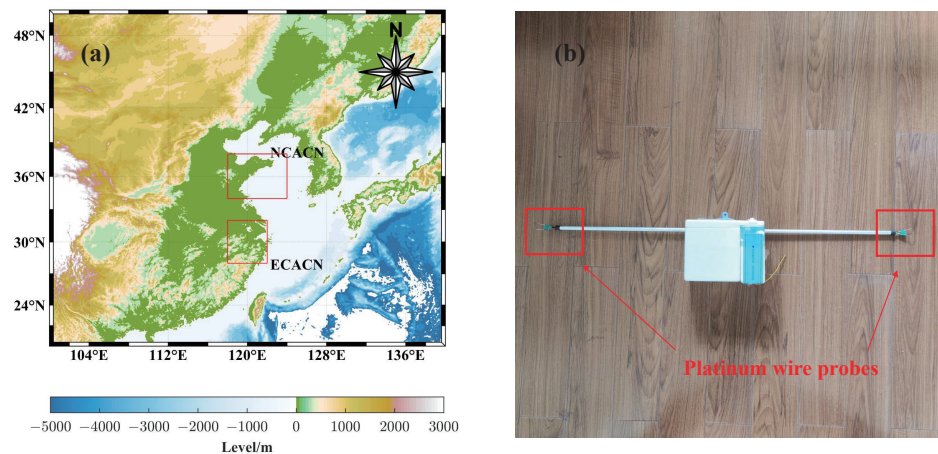


Figure 1. Field observation areas and instrument. (a) Sites locations: the eastern coastal area of China (ECACN) and the northern coastal area of China (NCACN). (b) Instrument: platinum wire probes (red rectangular boxes).

2.2. Scientific Data

The field observations were carried on two areas (Figure 1a) during April 2018. One observation was undertaken in the eastern coastal area of China (hereinafter ECACN), and the other in the northern coastal area of China (hereinafter NCACN). After removing several incomplete datasets with low termination altitude or missing data, we chose 16 and 20 profiles of ECACN and NCACN, respectively. The data collections of two areas are summarized in Table 1. More details are documented in Appendix B Tables A1 and A2.

Table 1. Radiosonde data collection of two areas.

Areas	Morning Launches	Evening Launches	Total Launches
ECACN	0	16	16
NCACN	9	11	20

3. Methodology of MEP

3.1. Theory of the Adopted Models

Seven different approaches (HV: Hufnagel-Valley 5/7; H9: Hmnsp99; DN: Dewan; TE: Thorpe; EN: Ellison; WT: WSPT; WG: WSTG) estimating C_n^2 with routine meteorological parameters were adopted in our study. We have summarized theories of these approaches in Appendix A to avoid interrupting the fluency of this article. More details can be found in the corresponding literature.

In data processing, all approaches except for HV involved gradient variables (the measured meteorological parameters or their derived parameters). Several approaches (TE, EN, and WT) calculated C_n^2 related to the sizes of localized overturns of the potential temperature. It was hard to distinguish these overturns for coarse resolution data because potential temperature profiles have an increasing tendency with height most of the time. Hence, we adopted the original resolution data in these approaches. Meanwhile, the other approaches (H9, DN, and WSTG) were calculated in the vertical resolution of 60 m. All seven approach estimations were re-processed on the scale of 60 m for consistency and convenience. Meanwhile, data exceeding 1 km above the ground level (AGL) were selected. Hence, the feature of C_n^2 and integrated astronomical parameters represent the free atmosphere results in our case.

3.2. MEP Method

Before introducing the principles of MEP, several theoretical basics should be elaborated first. For two variables, r and f , r_n is the reference variable (MT measured C_n^2 in this study), and f_n is the corresponding pattern result (estimated as C_n^2 in this study). The correlation coefficient (R) and their root-mean-square difference between two fields (E' , also known as the centered root-mean-square difference) are defined as:

$$R = \frac{\frac{1}{N} \sum_{n=1}^N (f_n - \bar{f})(r_n - \bar{r})}{\sigma_f \sigma_r}, \quad (3)$$

$$E' = \left\{ \frac{1}{N} \sum_{n=1}^N [(f_n - \bar{f}) - (r_n - \bar{r})]^2 \right\}^{1/2}, \quad (4)$$

where σ_r ($\sigma_r = 1/N \sqrt{\sum_{n=1}^N (r_n - \bar{r})^2}$) and σ_f ($\sigma_f = 1/N \sqrt{\sum_{n=1}^N (f_n - \bar{f})^2}$) denote the reference variable standard deviation and pattern result standard deviation, respectively; \bar{r} and \bar{f} represent the average of two variables. Thus, we can deduce the relationship between the reference standard deviation σ_r , pattern standard deviation σ_f , and correlation coefficient R as:

$$E'^2 = \sigma_f^2 + \sigma_r^2 - 2\sigma_f \sigma_r R, \quad (5)$$

Taylor devised the Taylor diagram to provide a concise statistical summary of how well the patterns match each other in terms of the above four statistics (σ_r , σ_f , R and E') [38]. In our study, we have normalized the statistics ($\hat{\sigma}_f = \sigma_f / \sigma_r$, $\hat{\sigma}_r = 1$, $\hat{E}' = E' / \sigma_r$) referring

to σ_r for convenience. According to Taylor's work, a skill function was also developed to assess the models' performance as follows:

$$S(\alpha, \beta) = \frac{2^\alpha (1 + R)^\beta}{\left(\hat{\sigma}_f + 1/\hat{\sigma}_f\right)^\alpha (1 + R_0)^\beta}, \quad (6)$$

where R_0 represents the maximum of R in a set of the same model and we set $R_0 = 1$; α and β are penalty coefficients that can adjust the proportion of skill function via model variance and correlation coefficient. A more considerable value of α or β means that the corresponding statistic ($\hat{\sigma}$ or R) has a more significant influence on the result of $S(\alpha, \beta)$.

Further, a weight function is defined as:

$$W_j(\gamma) = \frac{S_j^\gamma}{\sum_{i=1}^N S_i^\gamma}. \quad (7)$$

Note that all skill values are in the range of 0–1. We set a penalty parameter γ to distinguish the model's performance. Consequently, the multi-model ensemble pattern (MEP) method process is divided into three steps, as shown in Figure 2. We have summarized them as follows:

1. Using routine meteorological parameters estimating C_n^2 with multiple models;
2. Obtaining models skills $S(\alpha, \beta)$ against MT results in Equation (6);
3. Calculating weights $W_j(\gamma)$ of different models and MEP results.

Meanwhile, parameters (α, β) are used for modulating the weights of different statistics, and γ is used to distinguish the different models' performance. These penalty parameters can be changed as the research focus changes in practice. For example, we can increase the α value to increase the weight of data fluctuation in the evaluation system. It is the same for the β for correlations, and we chose the latter condition in our case. Moreover, a considerable γ means a more significant influence on the evaluation of skills. In our case, we set $\alpha = 2, \beta = 6, \gamma = 4$.

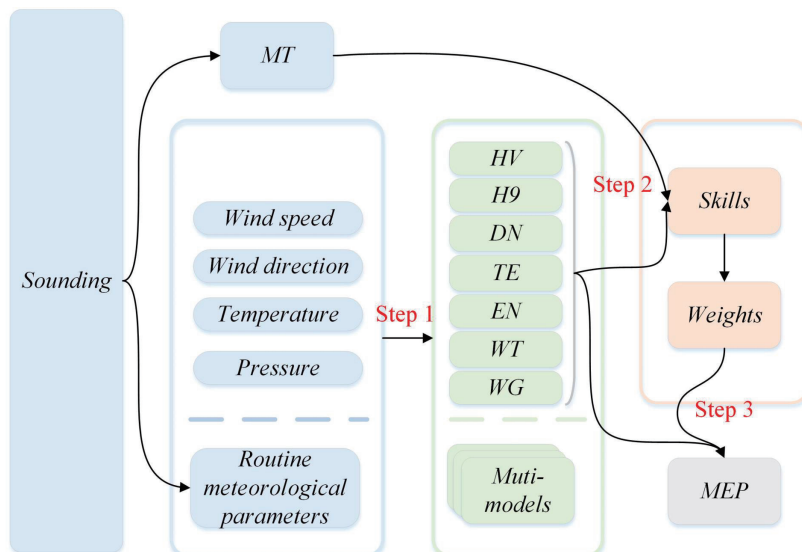


Figure 2. Process of MEP. Abbreviation meanings are as follows after this. MT: micro-thermal; HV: Hufnagel-Valley 5/7; H9: Hmnsp99; DN: Dewan; TE: Thorpe; EN: Ellison; WT: WSPT; WG: WSTG; MEP or ME: multi-model ensemble pattern method.

3.3. Statistical Analysis

In addition to the correlation coefficient (R), the root mean square error ($RMSE$), bias ($Bias$), and mean absolute error (MAE) were calculated to evaluate the performance of the different approaches. The definitions of these statistics are as follows:

$$RMSE = \sqrt{\frac{1}{N} \sum_{n=1}^N (r_n - f_n)^2}, \quad (8)$$

$$Bias = \frac{1}{N} \sum_{n=1}^N (r_n - f_n), \quad (9)$$

$$MAE = \frac{1}{N} \sum_{n=1}^N |r_n - f_n|. \quad (10)$$

4. Results and Discussion

4.1. Measured and Estimated C_n^2 Profiles

We employed 16 and 20 radiosonde datasets of two areas when evaluating the performance of the proposed and adopted methods. We used $\log_{10}(C_n^2)$ instead of C_n^2 to generate readable data and curves. We provide two C_n^2 profiles of all approaches against the MT of each dataset in the primary text. See Appendix B for all days details in two sites (Figures A1–A3 in ECACN; Figures A4–A7 in NCACN).

Figure 3a,b displays MT and estimations C_n^2 profiles from the ECACN radiosonde campaign. The overall trends of estimations are consistent with MT. The C_n^2 magnitude of estimations and MT are mainly distributed in the range of $10^{-15} – 10^{-19} m^{-2/3}$. Distinct differences can also be seen between different estimations. HV has a very high correlation with MT within the troposphere. However, it underestimates C_n^2 significantly above approximately 20 km, which indicates that a more turbulent and complex atmospheric state might exist above the troposphere in this area. TE, EN, and WT have better performance in magnitude owing to the calibration of unknown proportionality constants according to MT measurements. H9, DN, and WG have a similar trend in the overall trend, while these estimations fluctuate a little bit more around the mean value against TE, EN, WT, and ME. By combining the corresponding Taylor diagrams in Figure 3c,d, we can also easily find that the values of normalized standard deviations of HV, H9, DE, and WG are much bigger than MT most of the time. Meanwhile, closer normalized standard deviation values to 1 (or MT) of TE, EN, and ME means that these approaches have similar behavior in C_n^2 fluctuation magnitude. In addition, ME also shows its advantage in correlation evaluation. Among all 16 launches, correlation coefficients between ME and MT are mainly distributed around 0.6–0.8 and the best one is up to approximately 0.9.

Figures A1–A3 in Appendix B display all the C_n^2 profiles in ECACN. Scatter figures of all approaches against MT for all launches were plotted to further study the overall statistical features. Figure 4 shows all launches estimated C_n^2 statistical feature in ECACN. The relevant statistics are summarized in Table 2. Although the overall $Bias$ of ME is slightly larger than WT, R , MAE and $RMSE$ of ME present the best performance of all approaches.

Table 2. ECACN 16 C_n^2 profiles statistics.

Statistics	HV	H9	DN	TE	EN	WT	WG	ME
R	0.64	0.61	0.53	0.60	0.63	0.53	0.60	0.65
$Bias$	0.60	0.57	0.08	-0.30	0.18	-0.005	-0.15	-0.11
MAE	0.81	0.73	0.76	0.56	0.53	0.54	0.64	0.51
$RMSE$	1.13	0.92	0.95	0.70	0.67	0.68	0.81	0.64

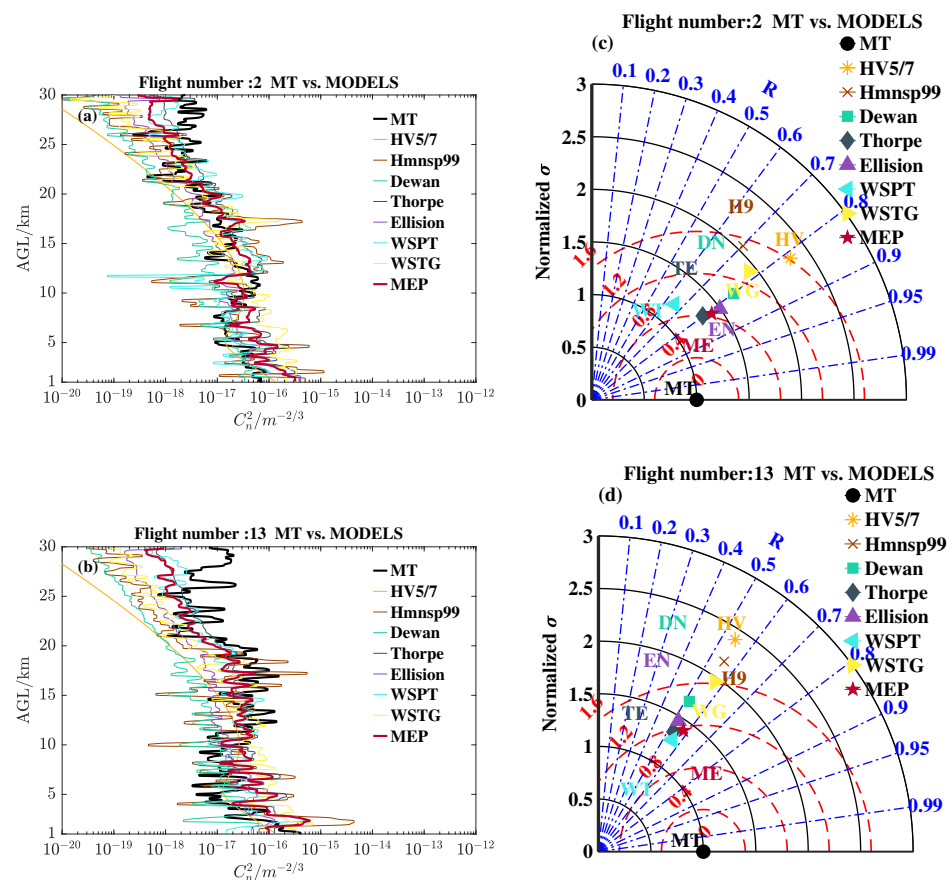


Figure 3. Measured and estimated C_n^2 profiles in ECACN. (a,b): single day C_n^2 profiles; (c,d): corresponding Taylor diagram of a single day C_n^2 statistics. The black solid curves in circles mark MT and models normalized standard deviation $\hat{\sigma}$; the blue dashed lines mark the correlation coefficient R ; the red dashed lines mark the root-mean-square difference E' between the models and MT. Intuitively, the closer the model is to the reference (MT, the black circle solid point) in the diagram, the better the estimation is.

Validation was also done to the radiosonde data from the campaign carried out in NCACN. Twenty sounding datasets were selected in this area. Figure 5 exhibits two launches C_n^2 profiles and their corresponding Taylor diagrams. The characteristics of different approaches estimation profiles are similar to those in ECACN. MEP correlation coefficients of a single launch in NCACN are mainly distributed around 0.7–0.9, and the best one is more than 0.95. Figures A4–A7 in Appendix B display all the C_n^2 profiles in NCACN. Figure 6 shows all 20 launches estimated C_n^2 against the MT statistical feature in NCACN. The relevant statistics are summarized in Table 3. The overall correlation criteria R of MEP is the best of all approaches, up to 0.7632. Meanwhile, the deviation criteria $Bias$, MAE , and $RMSE$ of MEP are the smallest. The above results of all the approaches in ECACN and NCACN have proved the potential of MEP in estimating C_n^2 utilizing radiosonde data.

Table 3. NCACN 20 C_n^2 profiles statistics.

Statistics	HV	H9	DN	TE	EN	WT	WG	ME
R	0.69	0.72	0.62	0.74	0.75	0.64	0.73	0.76
$Bias$	0.52	0.61	0.06	-0.22	0.26	0.02	-0.13	-0.09
MAE	0.74	0.71	0.73	0.49	0.49	0.52	0.56	0.45
$RMSE$	1.01	0.89	0.90	0.62	0.64	0.66	0.69	0.58

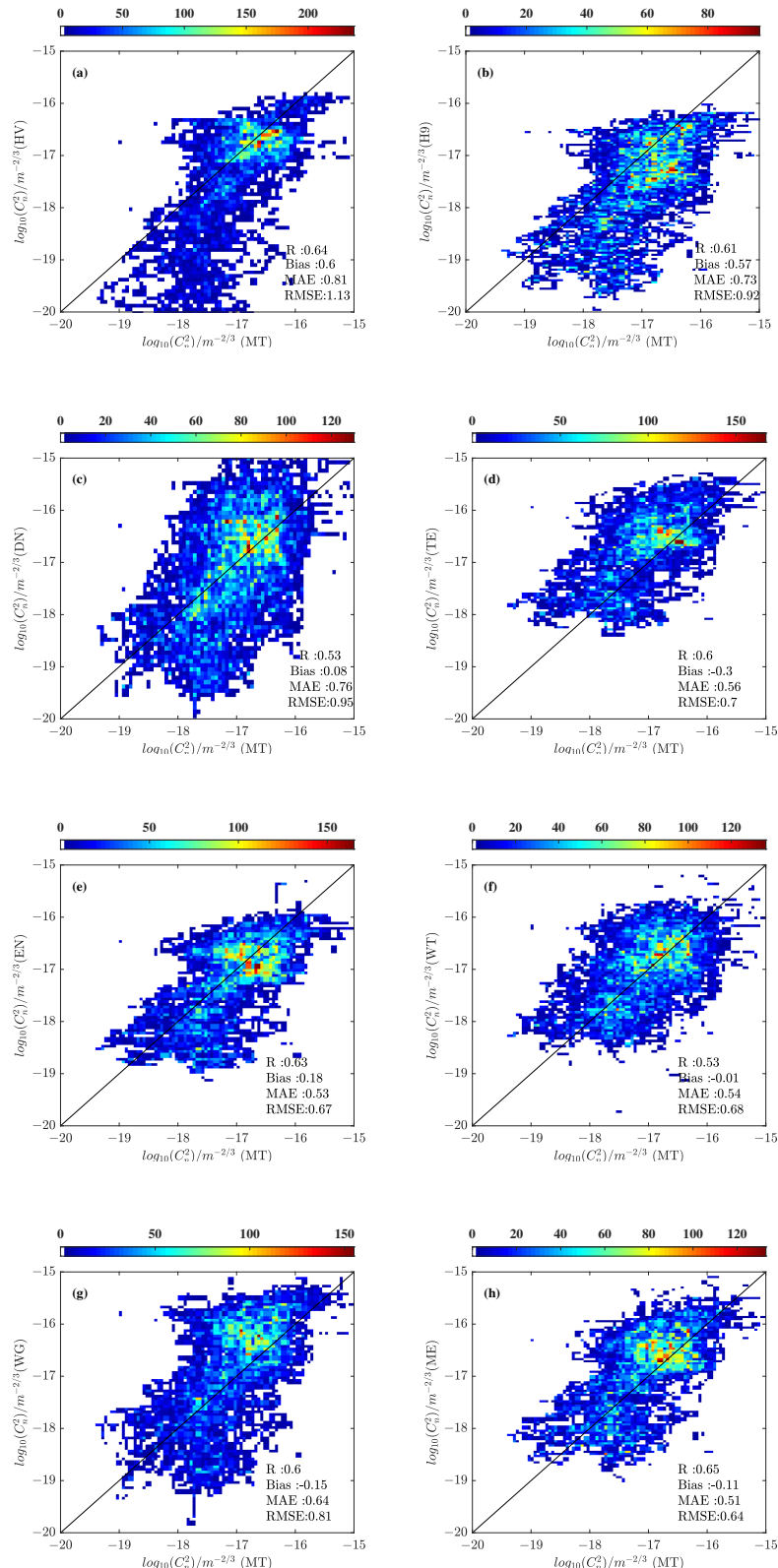


Figure 4. ECACN all launches MT vs. estimations C_n^2 scatter diagrams. **(a)**: MT vs. Hafnagel-Valley 5/7; **(b)** MT vs. Hmnsp99; **(c)**: MT vs. Dewan; **(d)**: MT vs. Thorpe; **(e)**: MT vs. Ellison; **(f)**: MT vs. WSPT; **(g)**: MT vs. WSTG; **(h)**: MT vs. MEP. The color indicates the frequency distribution of C_n^2 .

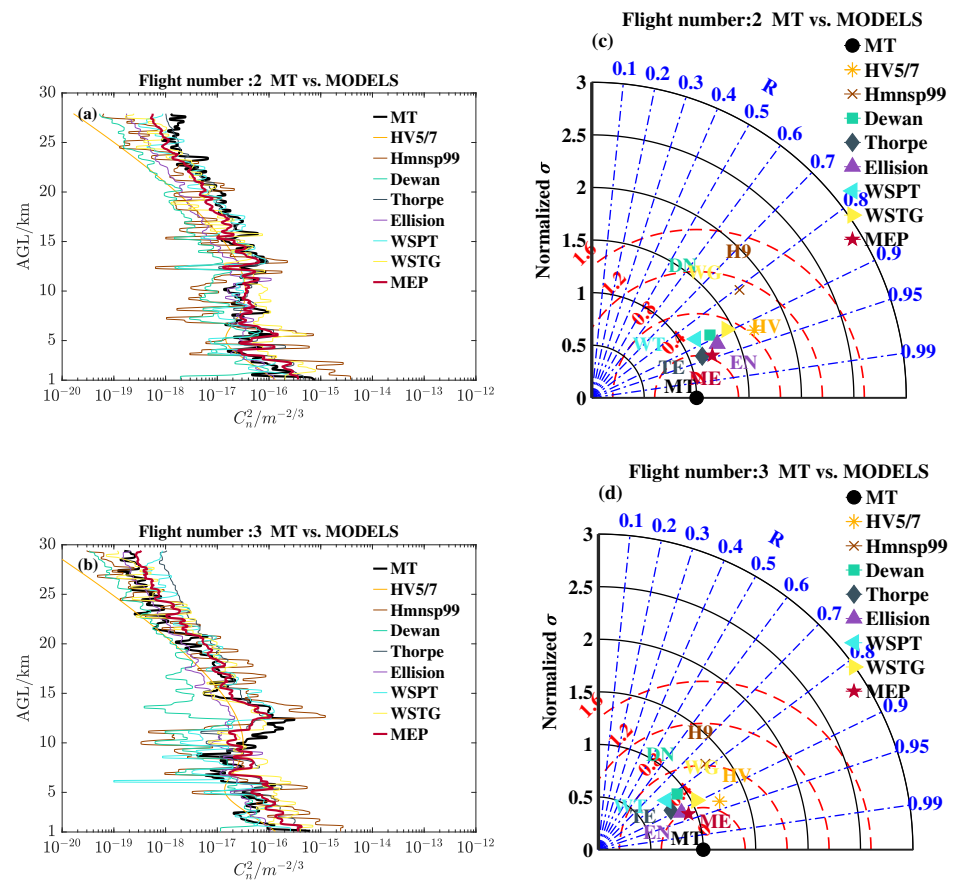


Figure 5. Measured and estimated C_n^2 profiles in NCACN. (a,b) A single day C_n^2 profiles; (c,d) corresponding Taylor diagram of a single day C_n^2 statistics.

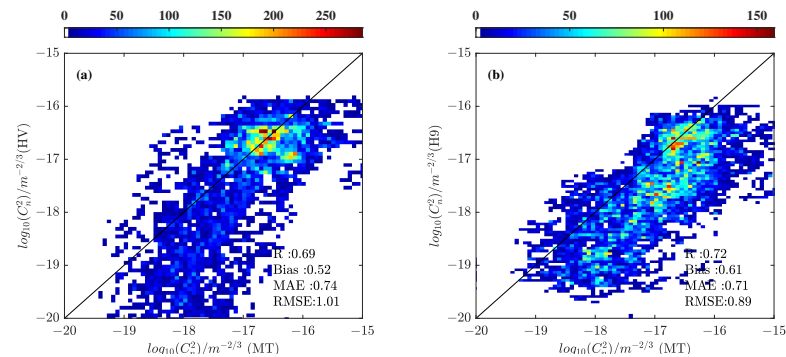


Figure 6. Cont.

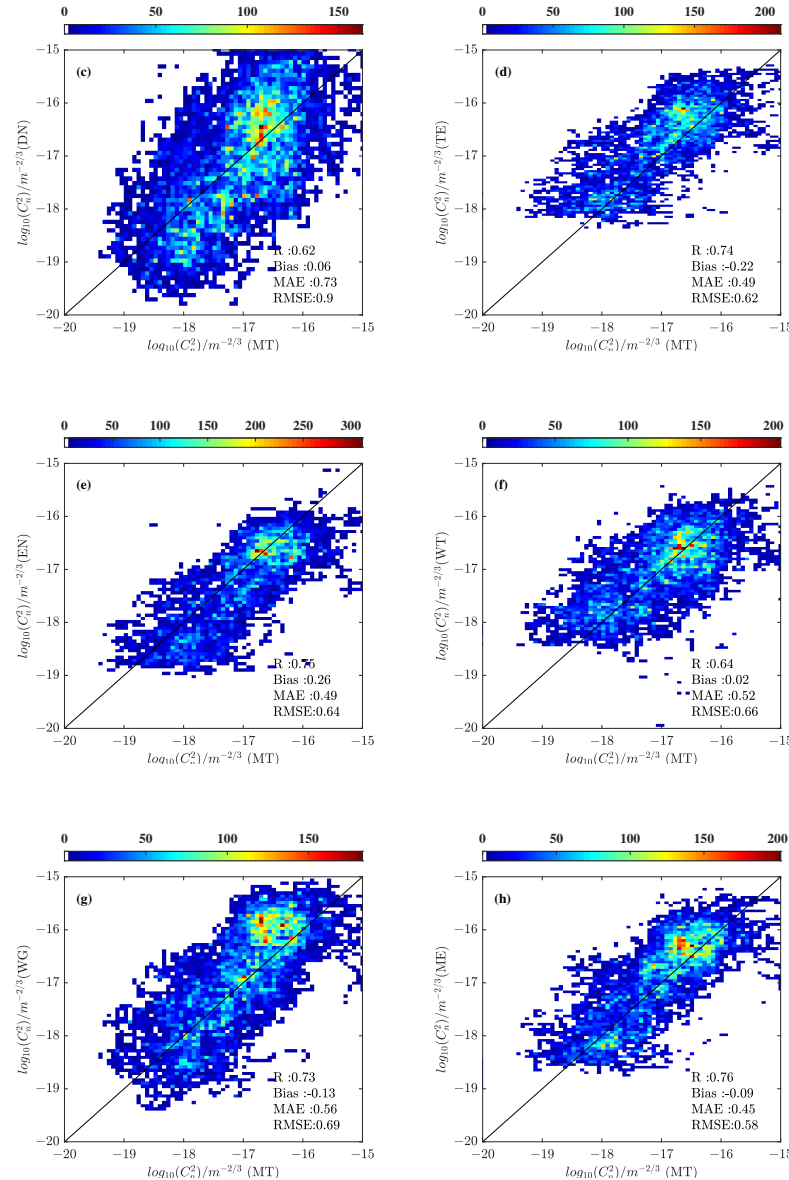


Figure 6. NCACN all launches MT vs. estimations C_n^2 scatter diagram. (a–h) The same as Figure 4 but for NCACN.

4.2. Integrated Astronomical Parameters from Measured and Estimated C_n^2 Profiles

Evaluating the optical turbulence influence on optoelectronic facilities (ground-based observatories, laser transmission, and free atmosphere optical communication systems) in the atmosphere is one of the primary aims of researchers. Hence, we also calculated the integrated astronomical parameters (Fried parameter r_0 , seeing ϵ , isoplanatic angle θ_{AO} and scintillation rate σ_I^2) to evaluate the performance of the proposed method. These parameters are defined as [5,9,12]:

$$r_0 = \left[0.423 \left(\frac{2\pi}{\lambda} \right)^2 \sec \varphi \int_{h_0}^{\infty} C_n^2(h) dh \right]^{-3/5}, \quad (11)$$

$$\epsilon = 5.25\lambda^{-1/5} \left[\int_{h_0}^{\infty} C_n^2(h) dh \right]^{3/5}, \quad (12)$$

$$\theta_{AO} = 0.057\lambda^{6/5} \left[\int_{h_0}^{\infty} C_n^2(h) h^{5/3} dh \right]^{-3/5}, \quad (13)$$

$$\sigma_I^2 = 19.12\lambda^{-7/6} \int_{h_0}^{\infty} C_n^2(h) h^{5/6} dh. \quad (14)$$

φ is the solar zenith angle set as 0° ; λ is a given wavelength (we set $\lambda = 550$ nm); h denotes the elevation above ground level (AGL) of the sites; h_0 represents the initial elevation (we set $h_0 = 1000$ m). Therefore, the conclusions of the integrated astronomical parameters included in this study can only represent the influence of the free atmosphere.

Details of these integrated astronomical parameters of all launches in ECACN are listed in the Appendix B, Tables A3–A6. The median values represent regional features and are of referential value for photoelectric applications. Median values of r_0 , ϵ , θ_{AO} , and σ_I^2 calculated from MT are 10.10 cm, $1.10''$, $0.67''$, and $0.54''$, respectively. These parameters calculated from ME are 8.93 cm, $1.25''$, $0.73''$, and $0.56''$. The relative errors of median values are rather small. All the integrated astronomical parameters are depicted in Figure 7, and the relevant statistical feature of these parameters are summarized in Table 4. HV and DN overestimated r_0 and θ_{AO} and underestimated ϵ and σ_I^2 can be easily found both from the figures and their *Bias* from the table against MT. The ME correlation coefficients of R_0 , ϵ and σ_I^2 are quite good. Meanwhile, the deviations are rather small compared to the other approaches.

Table 4. ECACN integrated astronomical parameters statistics (@ $\lambda = 550$ nm).

	Statistics	HV	H9	DN	TE	EN	WT	WG	ME
r_0	R	0.46	0.32	0.70	0.61	0.46	0.62	0.46	0.69
	<i>Bias</i>	-4.07	6.50	-8.87	4.56	-1.23	0.005	5.17	3.13
	<i>MAE</i>	5.01	6.60	8.87	4.89	4.17	3.27	5.31	4.01
	<i>RMSE</i>	6.11	8.13	9.86	6.48	4.79	4.28	7.17	5.32
ϵ	R	0.14	0.34	0.53	0.53	0.44	0.65	0.40	0.51
	<i>Bias</i>	0.39	-1.14	0.57	-0.45	0.15	0.15	-0.56	-0.20
	<i>MAE</i>	0.42	1.17	0.57	0.54	0.39	0.29	0.60	0.38
	<i>RMSE</i>	0.58	1.37	0.70	0.58	0.52	0.39	0.69	0.42
θ_{AO}	R	0.45	-0.42	0.56	0.49	0.45	0.29	0.03	0.38
	<i>Bias</i>	-0.59	0.35	-0.95	0.21	-0.28	0.05	0.21	0.08
	<i>MAE</i>	0.66	0.43	0.97	0.30	0.41	0.28	0.31	0.28
	<i>RMSE</i>	0.74	0.59	1.03	0.45	0.47	0.40	0.47	0.40
σ_I^2	R	0.14	-0.08	0.51	0.72	0.62	0.40	0.31	0.50
	<i>Bias</i>	0.37	-0.87	0.47	-0.21	0.25	0.14	-0.28	-0.004
	<i>MAE</i>	0.38	1.01	0.47	0.33	0.29	0.27	0.40	0.28
	<i>RMSE</i>	0.53	1.18	0.60	0.37	0.39	0.38	0.46	0.34

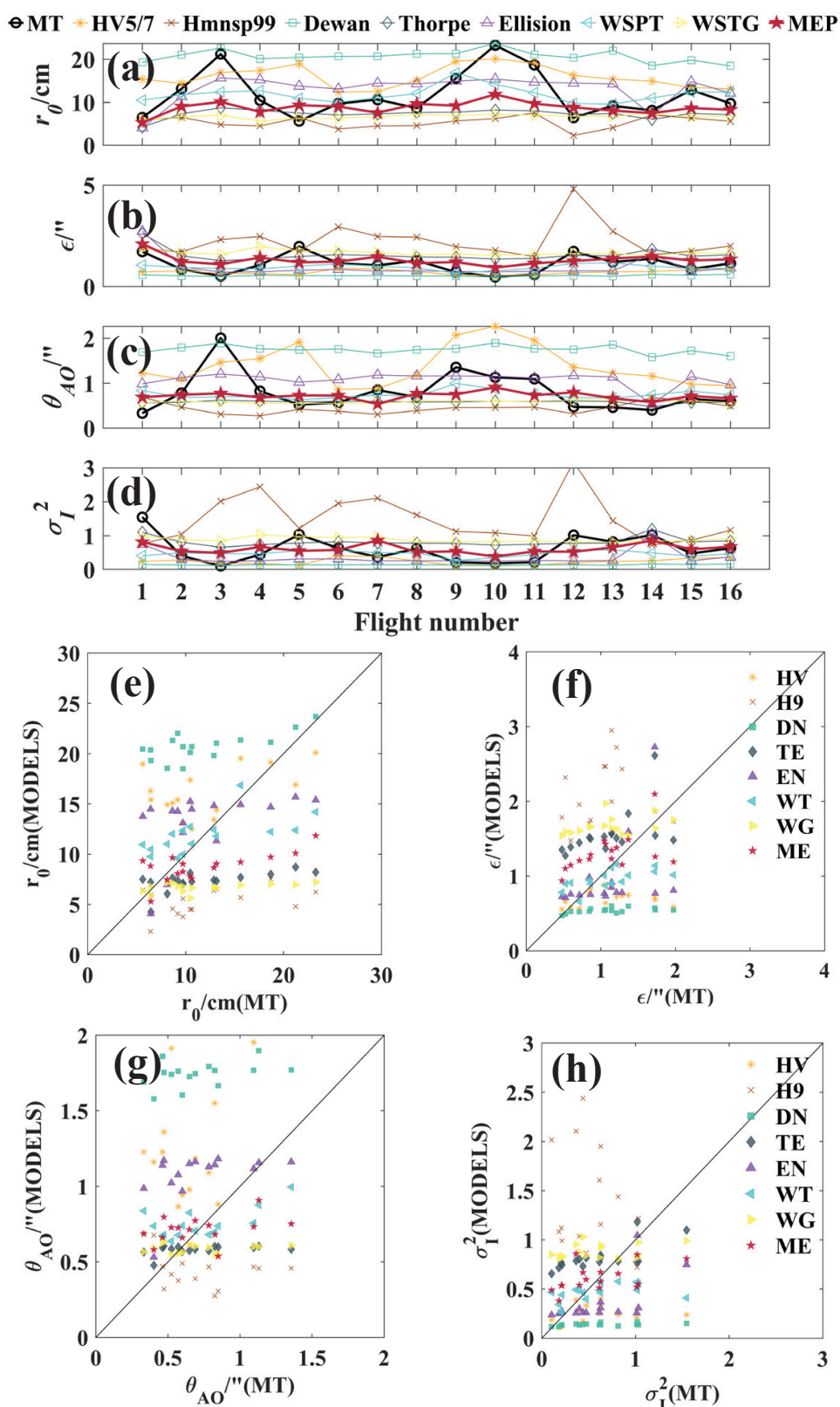


Figure 7. ECACN integrated astronomical parameters (@ $\lambda = 550$ nm). (a) Fried parameter r_0 (in cm); (b) seeing ϵ (arcsec in ''); (c) isoplanatic angle θ_{AO} (arcsec in ''); (d) scintillation rate σ_I^2 ; (e–h): corresponding scatter diagram.

The same computation process was done for the 20 radiosonde data from NCACN. The parameters calculated in NCACN are listed in the Appendix B, Tables A7–A10. Median

values of r_0 , ϵ , θ_{AO} , and σ_I^2 calculated from MT are 10.31 cm, 1.08'', 0.63'', and 0.66'', respectively. The parameters calculated from ME are 8.83 cm, 1.26'', 0.72'', and 0.58''. All the integrated astronomical parameters are portrayed in Figure 8, and the relevant statistical feature of these parameters are summarized in Table 5. The features of these parameters' statistics are similar to the results in ECACN. The ME correlation coefficients of all parameters are even better in general compared to ECACN. Meanwhile, the deviation statistics are relatively small overall compared to the other approaches. A comprehensive comparison in two experimental areas between MT and the best estimations of all the parameter statistics were summarized in Table 6. Although MEP is not always the best estimation among these eight approaches, its gap with the optimal approach is minimal. All the above show MEP's considerable universality in studying optical turbulence characteristics.

Table 5. NCACN integrated astronomical parameters statistics (@ $\lambda = 550$ nm).

	Statistics	HV	H9	DN	TE	EN	WT	WG	ME
r_0	R	−0.22	0.51	−0.006	0.64	0.59	0.40	0.42	0.60
	$Bias$	−4.68	5.90	−9.75	2.46	−3.90	−1.42	4.11	1.74
	MAE	6.28	5.98	9.75	4.04	4.19	3.69	4.86	3.63
	$RMSE$	7.61	7.17	10.89	4.87	5.37	4.44	6.03	4.27
ϵ	R	−0.16	0.62	0.12	0.58	0.64	0.24	0.53	0.58
	$Bias$	0.63	−1.32	0.84	−0.007	0.58	0.43	−0.37	0.08
	MAE	0.72	1.40	0.84	0.60	0.60	0.57	0.76	0.55
	$RMSE$	1.09	1.60	1.20	0.80	0.95	0.94	0.88	0.75
θ_{AO}	R	0.01	0.03	−0.03	0.38	0.47	0.32	0.20	0.45
	$Bias$	−0.56	0.36	−1.07	0.11	−0.41	0.01	0.16	0.03
	MAE	0.67	0.41	1.07	0.29	0.43	0.29	0.29	0.29
	$RMSE$	0.85	0.52	1.13	0.36	0.51	0.33	0.38	0.32
σ_I^2	R	−0.07	0.81	−0.05	0.31	0.39	0.11	0.24	0.59
	$Bias$	0.69	−1.24	0.84	0.26	0.69	0.48	0.02	0.34
	MAE	0.76	1.31	0.84	0.64	0.69	0.64	0.69	0.60
	$RMSE$	1.36	1.54	1.42	1.16	1.31	1.24	1.13	1.11

Table 6. Performance of MEP/ME against the best one (within parentheses) (the integrated astronomical parameters were calculated for the wavelength of light at $\lambda = 550$ nm. The values retain two decimal places).

Areas	Parameters	R	$Bias$	MAE	$RMSE$
ECACN	C_n^2	0.65(0.65:ME)	−0.11(−0.005:WT)	0.51(0.51:ME)	0.64(0.64:ME)
	r_0	0.69(0.70:DN)	3.13(0.005:WT)	4.01(3.27:WT)	5.32(4.28:WT)
	ϵ	0.51(0.65:WT)	−0.20(0.15:EN)	0.38(0.29:WT)	0.42(0.39:WT)
	θ_{AO}	0.38(0.56:DN)	0.08(0.05:WT)	0.28(0.28:WT)	0.40(0.40:ME)
	σ_I^2	0.50(0.72:TE)	−0.004(−0.004:ME)	0.28(0.27:WT)	0.34(0.34:ME)
NCACN	C_n^2	0.76(0.76:ME)	−0.09(0.02:WT)	0.45(0.45:ME)	0.58(0.58:ME)
	r_0	0.60(0.64:TE)	1.74(−1.42:WT)	3.63(3.63:ME)	4.27(4.27:ME)
	ϵ	0.58(0.64:EN)	0.08(−0.007:TE)	0.55(0.55:ME)	0.75(0.75:ME)
	θ_{AO}	0.45(0.47:EN)	0.03(0.01:WT)	0.29(0.29:ME)	0.32(0.32:ME)
	σ_I^2	0.59(0.59:ME)	0.34(0.02:WG)	0.60(0.60:ME)	1.11(1.11:ME)

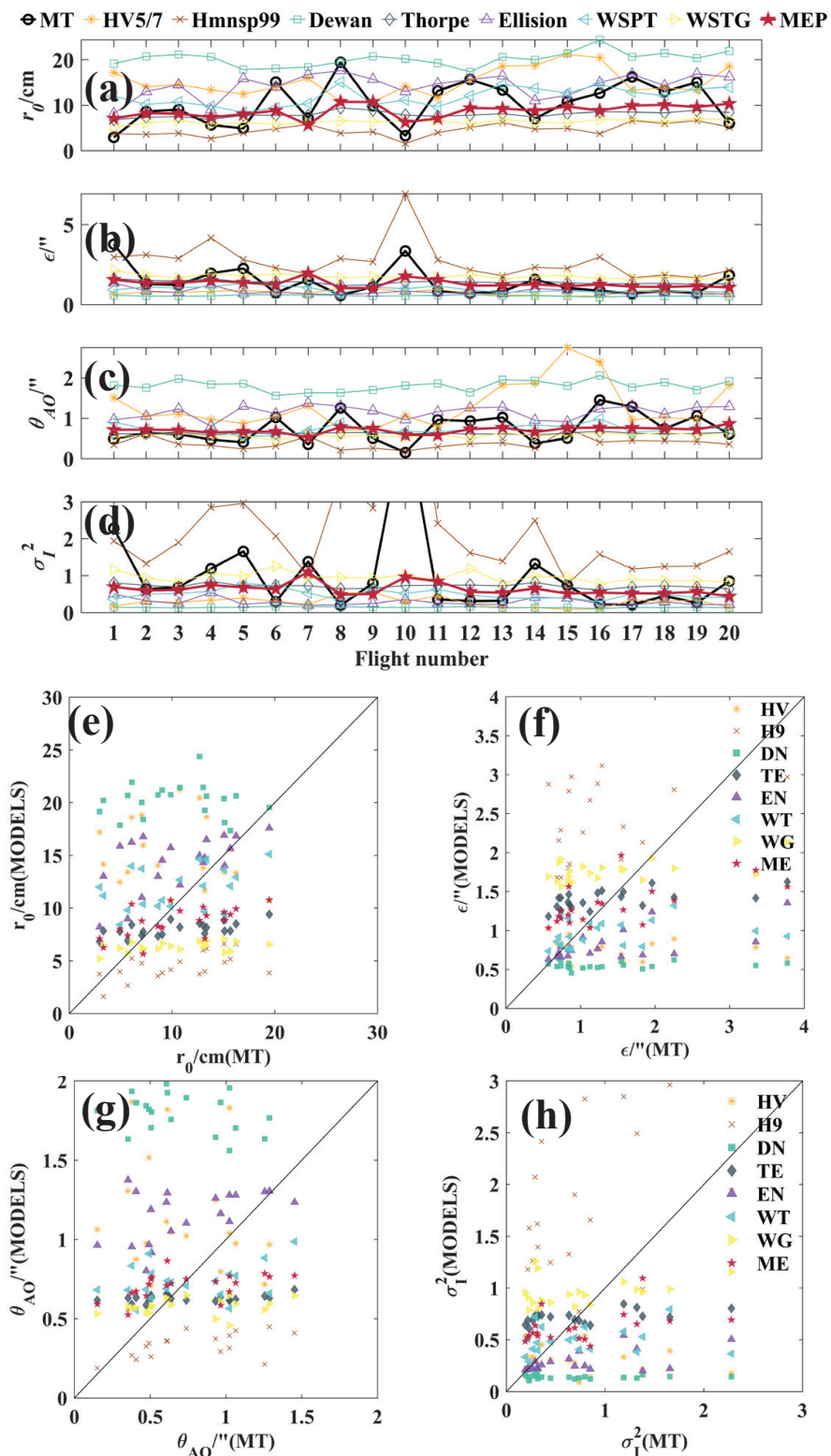


Figure 8. NCACN integrated astronomical parameters (@ $\lambda = 550 \text{ nm}$). (a) Fried parameter r_0 ; (b) seeing ϵ ; (c) isoplanatic angle θ_{AO} ; (d) scintillation rate σ_I^2 ; (e–h): corresponding scatter diagram.

5. Conclusions

In this study we propose a multi-model ensemble pattern method to estimate the C_n^2 based on several existing physical-based approaches. Balloon radiosonde data were collected in two areas of China to validate this method. Multiple dimensions evaluation

including C_n^2 and the integrated astronomical parameters (r_0 , ϵ , θ_{AO} and σ_I^2) of all approaches were done against the MT measured results. Statistical analysis of these methods' performance mainly focuses on the overall trend (R) and deviation (Bias, MAE, and RMSE). The best performance of all approaches against the MEP is summarized in Table 6. The C_n^2 correlation coefficients of MEP are up to 0.65 and 0.76. The overall agreements of the C_n^2 profiles in two areas are quite good. A single profile has an even higher correlation coefficient of more than 0.95. Several statistical assessments of deviations of C_n^2 are relatively small. These indicate that MEP has the capacity to estimate C_n^2 well. Meanwhile, the evaluations of integrated astronomical parameters also show its promising potential for calculating these parameters as C_n^2 does. Although MEP was not always the best method in all parameters statistical evaluations, it showed competitive performance in these evaluations. Hence, the MEP method presented good stability and universality, and even the validation radiosonde data were collected in different areas, which meant significantly different atmospheric conditions. The MEP appreciably contains more information than a single method, including thermodynamic and dynamic factors of the optical turbulence. Moreover, the MEP method could be less sensitive to different parametric settings caused by each method, producing a more robust C_n^2 estimate.

It should be noted that a single approach performed relatively well after well-designing the relevant parameters according to field radiosonde measurement in previous practice [21,28–30]. However, the designed parameters might be less effective for other sites. This weakness makes a single model challenging to extend without sufficient prior data. Reliable and universal methods estimating C_n^2 from routine meteorological parameters are critical to evaluate the optical turbulence influence on adaptive optics systems. The most obvious example is a forecasting study in which the astronomer can not obtain optical turbulence in advance directly. Generally, researchers can forecast C_n^2 via weather forecasting models, combining different estimating approaches [8,12,39,40]. In addition, it also provides us with an applicable method to study regional optical turbulence characteristics from historical meteorological data. To be certain, more validation work should be done up until that point.

Author Contributions: H.Z. ((Hanjiu Zhang): methodology, software, data analysis and writing—draft preparation; L.Z.: software, data analysis, and editing; G.S.: funding acquisition, guidance, data collection, data curation and writing—review; K.Z., Y.L., X.M. and H.Z. (Haojia Zhang): investigation and editing; Q.L.: instrument design and manufacture; S.C., T.L. and X.L.: funding acquisition, experiment guarantee, and data collection; N.W.: guidance and writing—review. All authors have read and agreed to the published version of the manuscript.

Funding: This research was funded by the National High-tech Research and Development Program (No. E23D0HA65S2).

Data Availability Statement: Data underlying the results presented in this paper are not publicly available at this time but may be obtained from the authors upon reasonable request.

Acknowledgments: The authors express their thanks to all AIOFM colleagues carrying out the experiments. The authors would like to thank the reviewers for their remarks and suggestions on the manuscript.

Conflicts of Interest: The authors declare no conflict of interest.

Abbreviations

The following abbreviations are used in this manuscript:

MEP or ME	Multi-model Ensemble Pattern
OT	Optical Turbulence
MT	Micro-thermometers
SLC	Submarine Laser Communication
ECACN	Eastern coastal area of China
NCACN	Northern coastal area of China
MASS	Multi-Aperture Scintillation Sensor
Slodar	Slope Detection And Ranging
S-Dimm+	Solar Differential Image Motion Monitor+
GPS	Global Positioning System
AGL	Above the ground level
HV5/7 or HV	Hufnagel-Valley5/7 Model
H9	Hmnsp99 Model
DN	Dewan Model
TE	Thorpe Model
EN	Ellison Model
WT	WSPT Model
WG	WSTG Model
AIOFM	Anhui Institute of Optics and Fine Mechanics

Appendix A. Theories of Adopted Approaches

Appendix A provides theories of adopted approaches estimating C_n^2 . We place the contents of Section 3.1 (primary manuscript) in this appendix document to avoid interrupting the fluency of the original article. In Section 3 (primary manuscript), we introduce several adopted physical-based approaches to estimate C_n^2 . Theories of these approaches are briefly summarized below in the appendix document. For more details, one may refer to the corresponding literature. We roughly classify these approaches into three types. The first type is the semi-physical and semi-statistical approach. The typical approach is the Hufnagel model. The second type focuses on the calculation of the turbulence outer scale. We adopted the Hmnsp99, Dewan, and wind shear and temperature gradient (WSTG) models. The third type estimates C_n^2 via the temperature structure parameter. The Thorpe, Ellison, and wind shear and potential temperature (WSPT) models are examples.

Appendix A.1. Hufnagel-Valley 5/7 Model

The Hufnagel-Valley model was developed based on the statics of radio sounding and stellar scintillation [22,23]. The most commonly used form is the Hufnagel-Valley 5/7 model related to wind speed. The calculated formula is expressed as:

$$C_n^2(h) = 8.2 \times 10^{-26} Wh^{10} e^{-h} + 2.7 \times 10^{-16} e^{-h/1.5} + Ae^{-h/0.1}, \quad (\text{A1})$$

where e is the Euler number; h (unit: m) is the height above the ground. In our case, the parameters $A = 1.7 \times 10^{-4}$ and $W = (1/15) \int_5^{20} V^2(h) dh$, where V is the wind speed (unit: m/s) between 5 and 20 km.

Appendix A.2. The Outer-Scale Method

Other approaches (Hmnsp99, Dewan, WSTG) estimating C_n^2 are based on the outer scale according to the work by Tatarskii [1]:

$$C_n^2 = 2.8L_0^{4/3}M^2, \quad (\text{A2})$$

where L_0 is the turbulence outer scale and M is the vertical gradient of the potential refractive index. The value of M^2 can be calculated from the temperature (T in K) and pressure (P in hPa) profiles as below:

$$M^2 = \left[\frac{-79 \times 10^{-6} P}{T^2} \left(\frac{d\theta}{dh} \right) \right]^2, \quad (\text{A3})$$

where θ (unit: K) is the potential temperature defined as $\theta = T(1000/P)^{0.286}$. Hence, the key to the C_n^2 estimation becomes the calculation of the outer scale. Most methods that parameterize the outer scale or turbulence with macroscopic quantities rely not only on the existing theoretical basis of turbulence but also on the statistics of large amounts of experiment and numerical simulation data and physical intuition and perspicacity of the founders of these models. The adopted approaches in our study calculating L_0 are listed below.

Appendix A.2.1. Hmnsp99 Model

The Hmnsp99 model defines L_0 with wind shear (S) and temperature gradients (dT/dh) [24]. The expressions are different in the troposphere and stratosphere as

$$L_0^{4/3} = \begin{cases} 0.1^{4/3} \times 10^{0.362+16.728S-192.347\frac{dT}{dh}}, & \text{Troposphere} \\ 0.1^{4/3} \times 10^{0.757+13.819S-57.784\frac{dT}{dh}}, & \text{Stratosphere} \end{cases} \quad (\text{A4})$$

where $S = \sqrt{(du/dh)^2 + (dv/dh)^2}$ (hereinafter), u and v are the north and east horizontal wind components, respectively.

Appendix A.2.2. Dewan Model

Dewan model deduces L_0 from only one parameter (wind shear) [25]. Meanwhile, it is similar to the Hmnsp99 model, which has a different form in the troposphere and stratosphere:

$$L_0^{4/3} = \begin{cases} 0.1^{4/3} \times 10^{1.64+42S}, & \text{Troposphere} \\ 0.1^{4/3} \times 10^{0.506+50S}. & \text{Stratosphere} \end{cases} \quad (\text{A5})$$

Appendix A.2.3. WSTG Model

The WSTG model is a modified model that comes from Hmnsp99. The calculation of the outer scale is related to the dynamic and thermodynamic state of the atmosphere [30]. The expression is as follows:

$$L_0^{4/3} = \begin{cases} 0.1^{4/3} \times 10^{0.835-37.464S-306.034\frac{dT}{dh}}, & S < 0.016 \cap dT/dh < 0 \\ 0.1^{4/3} \times 10^{0.825+66.9S-52.783\frac{dT}{dh}}, & S < 0.016 \cap dT/dh > 0 \\ 0.1^{4/3} \times 10^{0.715+52.907S-102.251\frac{dT}{dh}}, & S > 0.016 \cap dT/dh < 0 \\ 0.1^{4/3} \times 10^{2.215-9.882S-101.666\frac{dT}{dh}}, & S > 0.016 \cap dT/dh > 0 \end{cases} \quad (\text{A6})$$

Appendix A.3. The Temperature Structure Parameter Method

The remaining approaches (Thorpe, Ellison, WSPT) deduce C_n^2 from the Gladstone relationship [12] as follows:

$$C_n^2 = \left(79 \times 10^{-6} \frac{P}{T^2} \right)^2 C_T^2, \quad (\text{A7})$$

and the temperature structure parameter (C_T^2) expressed as:

$$C_T^2 = c_0 L_0^{4/3} \left(\frac{\partial \bar{\theta}}{\partial h} \right)^2. \quad (\text{A8})$$

c_0 is a constant that should be determined by experiment. $c1$, $c2$, and $c3$ are also unknown proportionality constants determined by experiment data in the following Equations (A9), (A11), and (A13).

Appendix A.3.1. Thorpe Model

The Thorpe model quantifies C_T^2 with the Thorpe scale (L_T) and sorted potential temperature gradients ($\partial \theta_s / \partial h$) [26] as follows:

$$C_T^2 = c_1 L_T^{4/3} \left(\frac{\partial \theta_s}{\partial h} \right)^2, \quad (\text{A9})$$

$$L_T = \begin{cases} \sqrt{|h_{original} - h_{sorted}|} \\ \text{or} \\ |h_{original} - h_{sorted}| \end{cases}. \quad (\text{A10})$$

θ_s (hereinafter) is the sorted potential temperature rearranged in ascending order; $h_{original}$ and h_{sorted} are the corresponding heights of the original potential temperature and sorted potential temperature, respectively. In our case, we chose the latter formula of Equation (A10) to calculate L_T .

Appendix A.3.2. Ellison Model

Ellison proposed the Ellison scale, which refers to density or potential temperature, to study the overturning of fluid caused by turbulences [27,28]. The calculation formula is as follows:

$$C_T^2 = c_2 L_E^{4/3} \left(\frac{\partial \theta_s}{\partial h} \right)^2, \quad (\text{A11})$$

$$L_E = \left| \frac{\Delta \theta}{\partial \theta_s / \partial h} \right|. \quad (\text{A12})$$

L_E is the Ellison scale; $\Delta \theta$ (hereinafter) represents the difference value of the original and sorted (ascending) potential temperature.

Appendix A.3.3. WSPT Model

The WSPT model involves both the wind speed and potential temperature information, calculating C_T^2 [29] as follows:

$$C_T^2 = c_3 L_W^{4/3} \left(\frac{\partial \theta_s}{\partial h} \right)^2, \quad (\text{A13})$$

$$L_W = \sqrt{\frac{|\Delta \theta|}{\partial \theta_s / \partial h} \cdot \left(\frac{uv}{S^2} \right)^{1/2}}. \quad (\text{A14})$$

Appendix B. Details of Two Areas Radiosonde, Models Estimations, and Integrated Astronomical Parameters Results

This Appendix B provides the details of two areas radiosonde, models estimations, and integrated astronomical parameters results. Variables, symbols, and abbreviations used in this document have the same meanings as the primary manuscript.

Appendix B.1. Radiosonde Details

Appendix B.1.1. ECACN

Radiosonde details of the eastern coastal area of China (ECACN) are included in Table A1.

Table A1. ECACN radiosonde details (BJT: Beijing time).

Site	Flight Number	Date	Release Time (BJT)	Flight Duration /s	Termination Altitude (AGL)/m
ECACN	1	5 April 2018	19:30	5010	29,020
	2	9 April 2018	19:30	5027	31,210
	3	10 April 2018	19:30	4767	30,410
	4	11 April 2018	19:30	4788	27,880
	5	12 April 2018	19:30	5014	29,810
	6	15 April 2018	19:30	4088	25,740
	7	17 April 2018	19:30	4355	26,410
	8	18 April 2018	19:30	4686	28,150
	9	19 April 2018	19:30	5037	30,120
	10	20 April 2018	19:30	5371	31,620
	11	22 April 2018	19:30	4820	28,220
	12	24 April 2018	19:30	5176	30,710
	13	25 April 2018	19:30	5051	30,910
	14	26 April 2018	19:30	5088	29,410
	15	27 April 2018	19:30	5443	31,750
	16	28 April 2018	19:30	5144	31,170

Appendix B.1.2. NCACN

Radiosonde details of the northern coastal area of China (NCACN) are included in Table A2.

Table A2. NCACN radiosonde details.

Site	Flight Number	Date	Release Time (BJT)	Flight Duration /s	Termination Altitude (AGL)/m
NCACN	1	3 April 2018	19:30	4464	28,660
	2	4 April 2018	7:30	4210	27,970
	3	4 April 2018	19:30	4747	29,460
	4	5 April 2018	7:30	4808	29,320
	5	8 April 2018	19:30	4271	27,370
	6	9 April 2018	7:30	4855	28,880
	7	9 April 2018	19:30	4780	29,660
	8	10 April 2018	19:30	5275	29,780
	9	12 April 2018	7:30	4591	27,810
	10	13 April 2018	7:30	4633	28,710
	11	14 April 2018	19:30	5069	29,680
	12	16 April 2018	7:30	5360	29,380
	13	16 April 2018	19:30	5292	30,050
	14	17 April 2018	7:30	5176	28,850
	15	20 April 2018	7:30	5155	29,660
	16	21 April 2018	19:30	4853	29,400
	17	25 April 2018	19:30	5012	30,750
	18	26 April 2018	7:30	4714	28,790
	19	26 April 2018	19:30	4901	30,660
	20	27 April 2018	19:30	4798	28,530

Appendix B.2. The Refractive Index Structure Parameter of MT and Estimations

Appendix B.2.1. ECACN MT and Models Estimations

The refractive structure index parameter profiles of MT and estimations in ECACN are exhibited in Figures A1–A3.

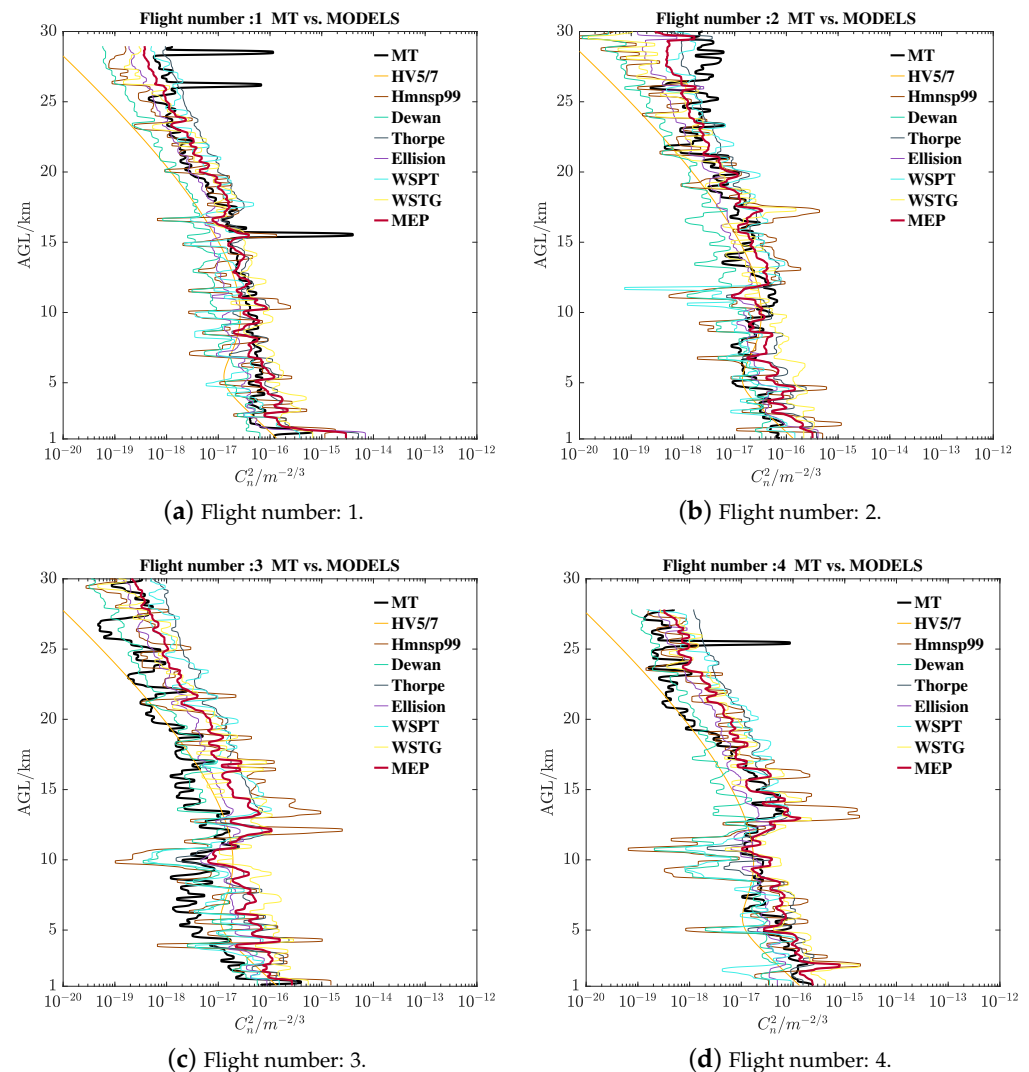


Figure A1. The refractive index structure parameter profiles of MT and estimations in ECACN: Figure A1 sub-figures (a–d) are flight numbers 1–4 in Table A1.

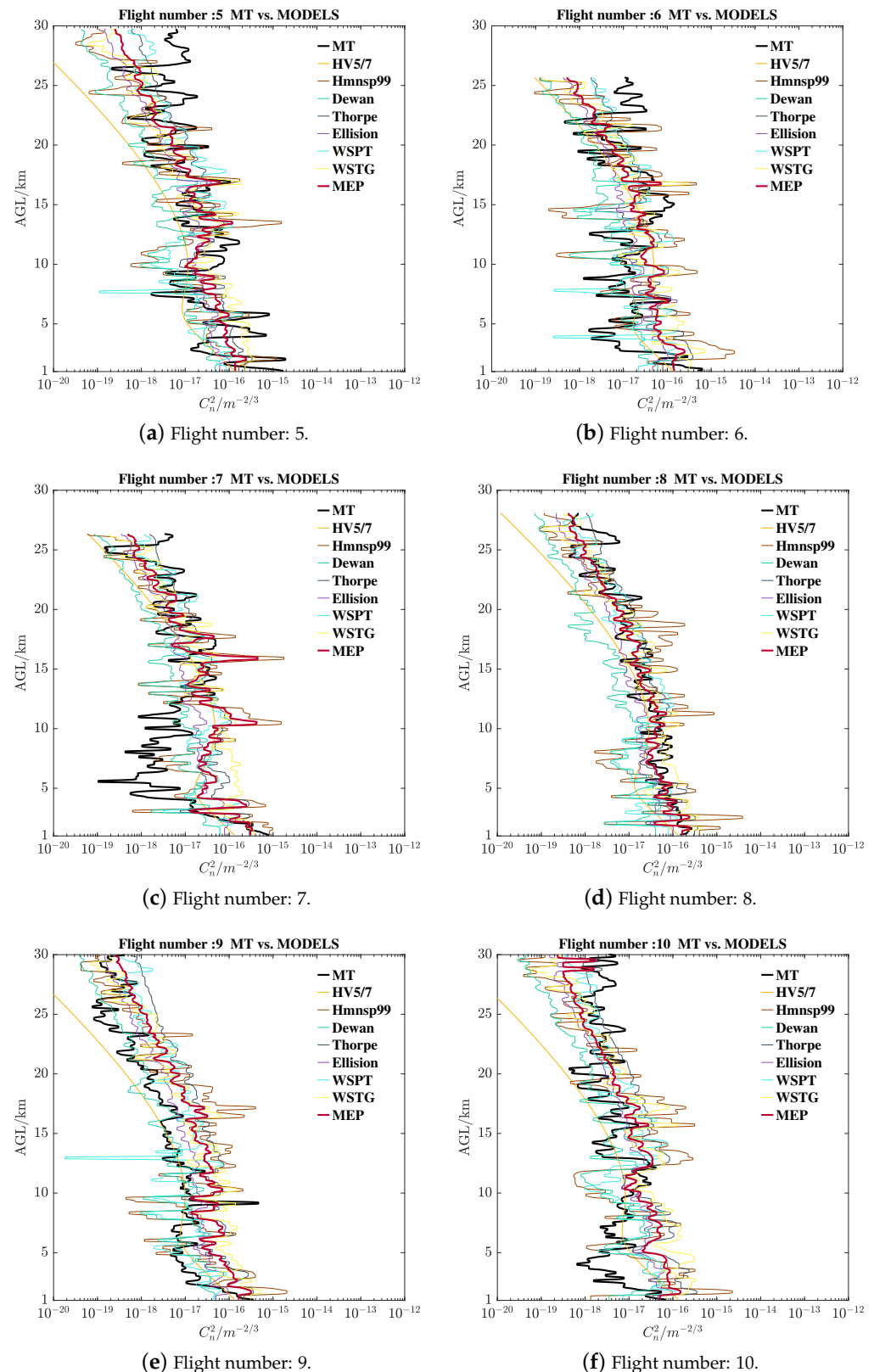


Figure A2. The refractive index structure parameter profiles of MT and estimations in ECACN: Figure A2 sub-figures (a–f) are flight numbers 5–10 in Table A1.

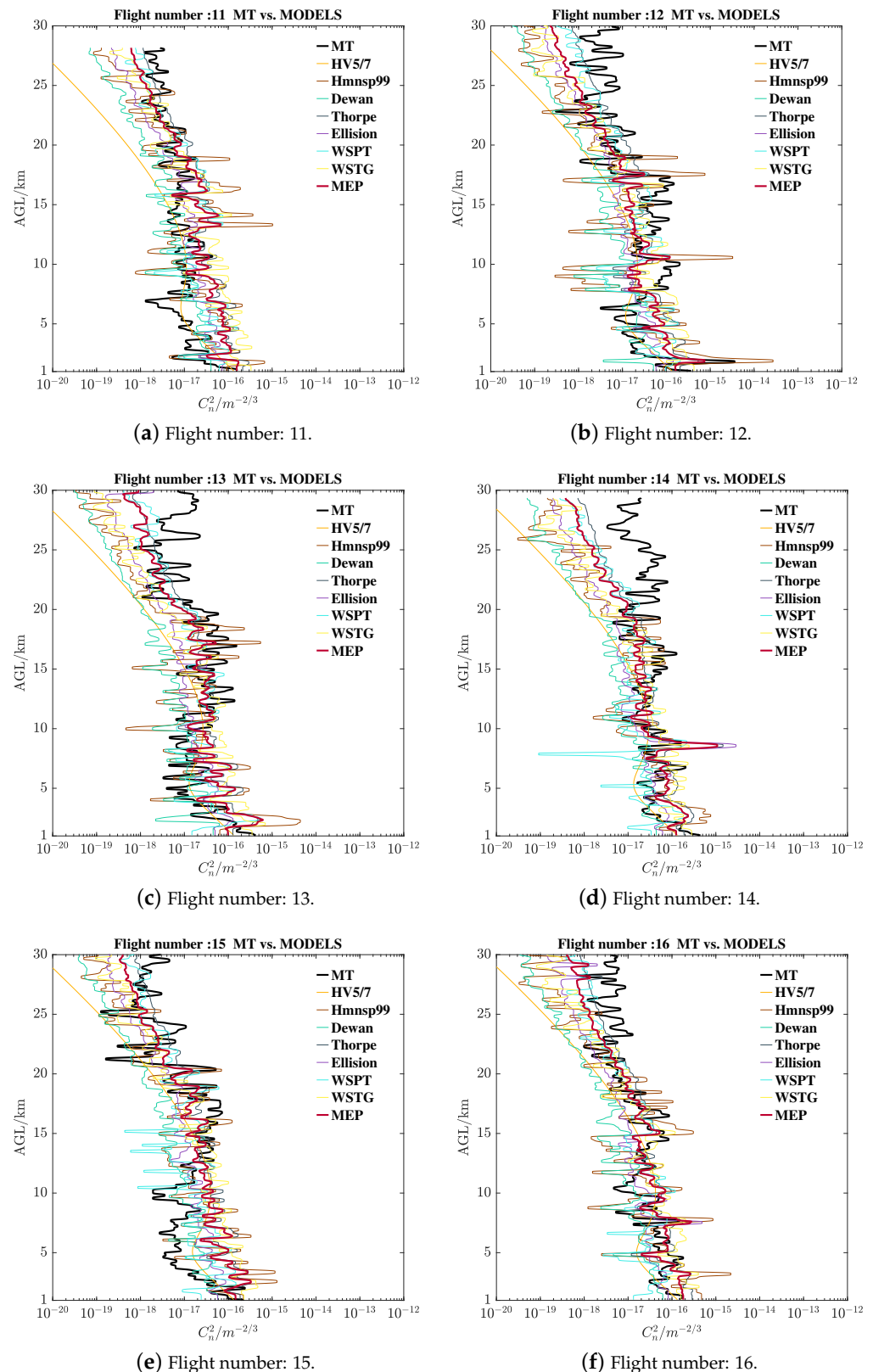


Figure A3. The refractive index structure parameter profiles of MT and estimations in ECACN: Figure A3 sub-figures (a–f) are flight numbers 11–16 in Table A1.

Appendix B.2.2. NCACN MT and Models Estimations

The refractive structure index parameter profiles of MT and estimations in NCACN are exhibited in Figures A4–A7.

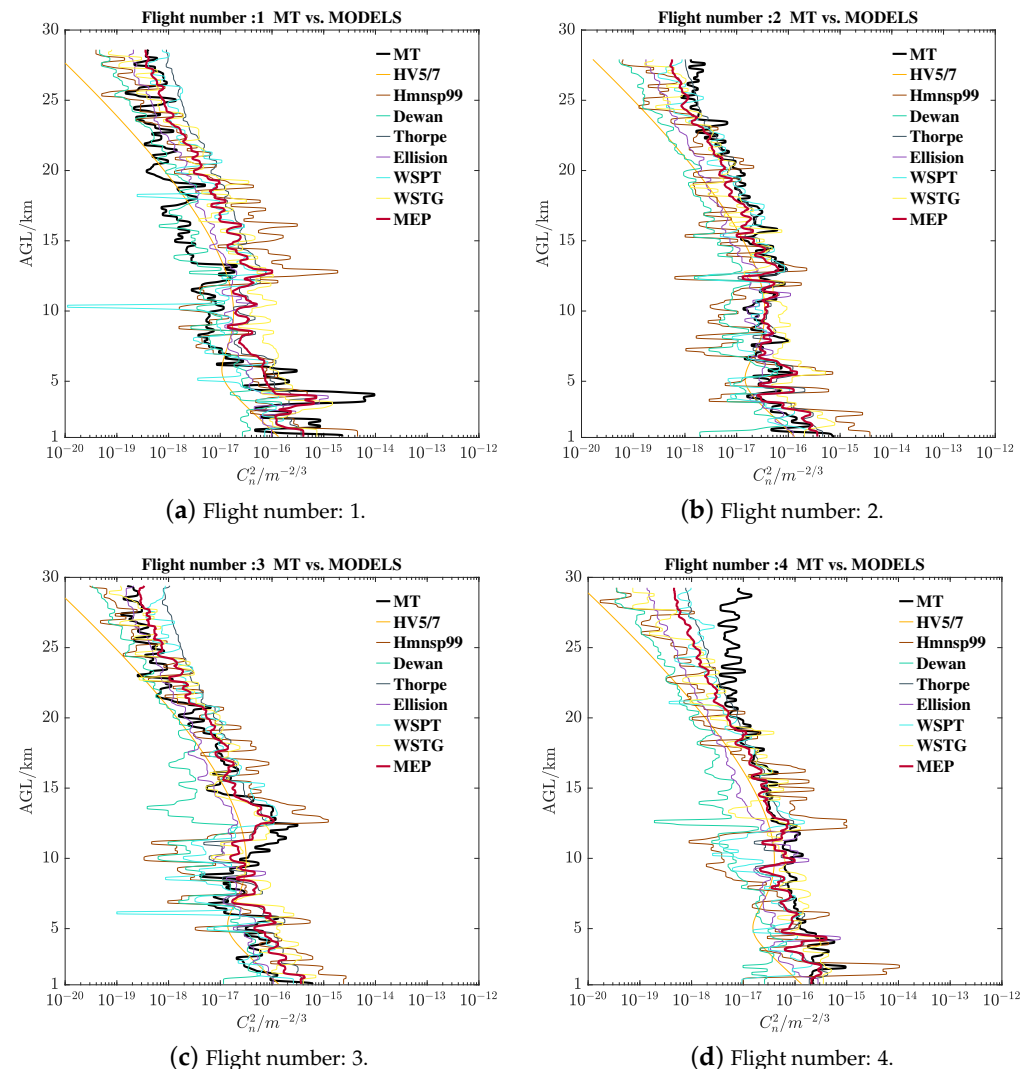


Figure A4. The refractive index structure parameter profiles of MT and estimations in NCACN: Figure A4 sub-figures (a–d) are flight numbers 1–4 in Table A2.

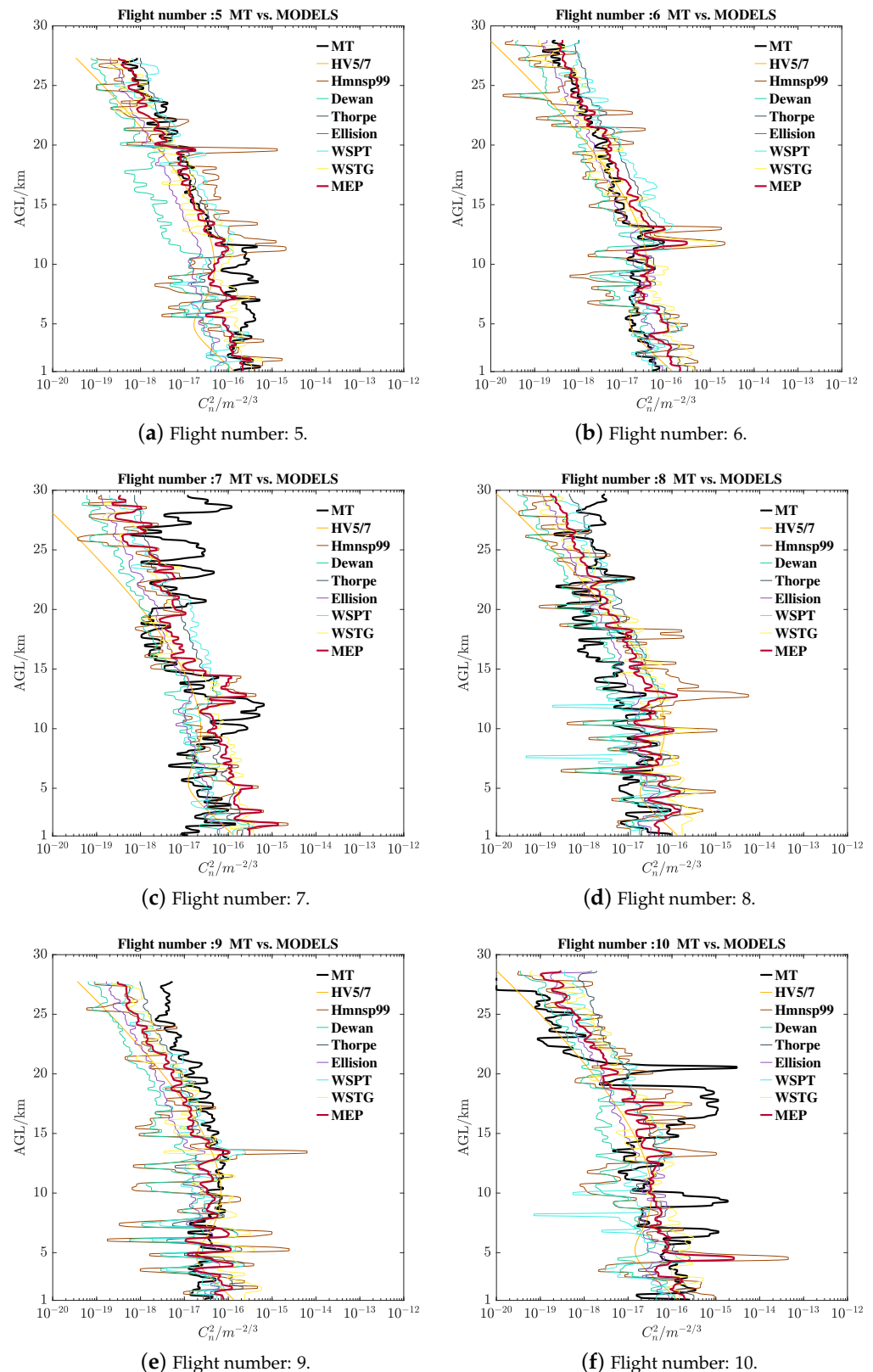


Figure A5. The refractive index structure parameter profiles of MT and estimations in NCACN: Figure A5 sub-figures (a–f) are flight numbers 5–10 in Table A2.

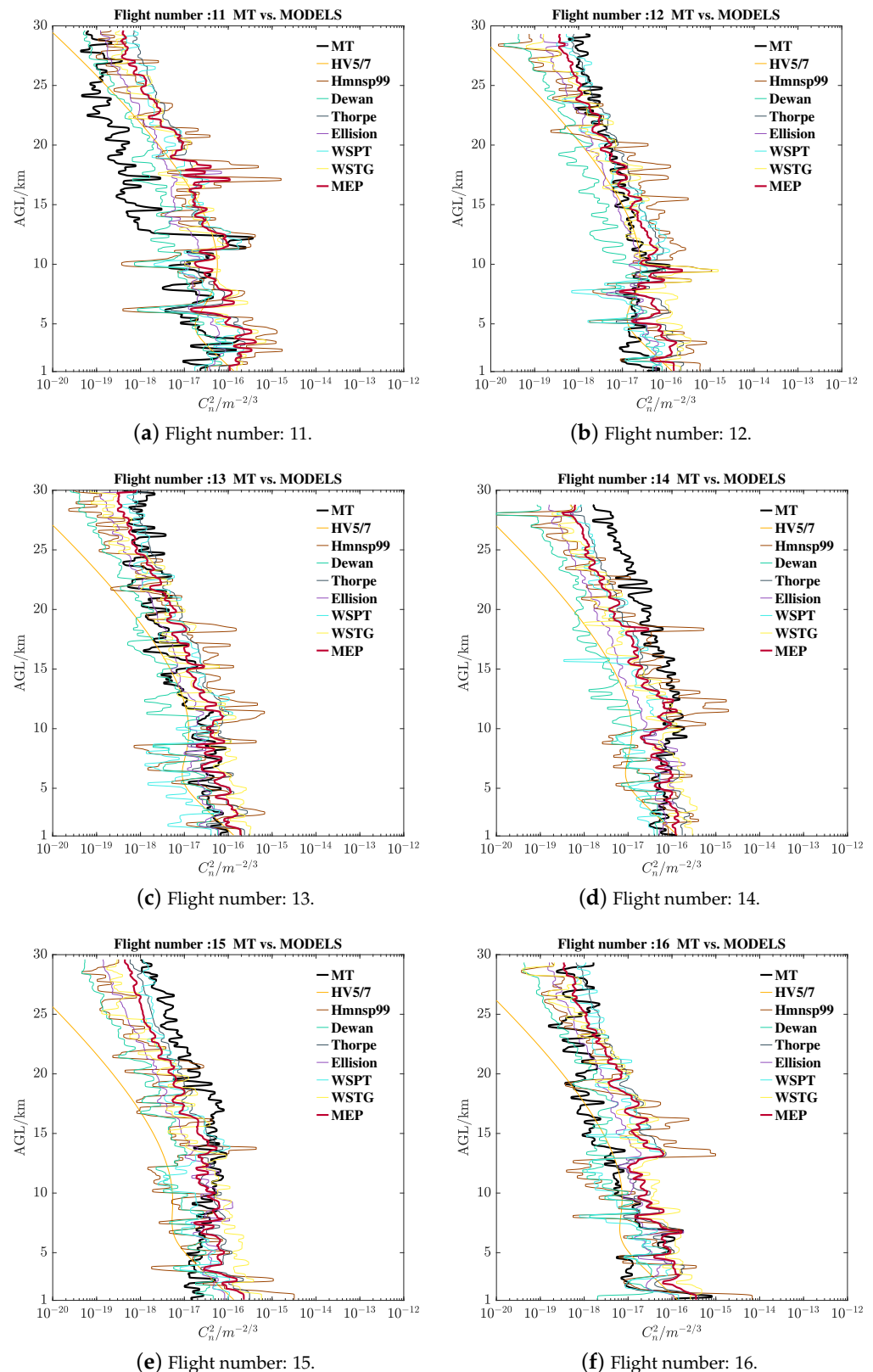


Figure A6. The refractive index structure parameter profiles of MT and estimations in NCACN: Figure A6 sub-figures (a–f) are flight numbers 11–16 in Table A1.

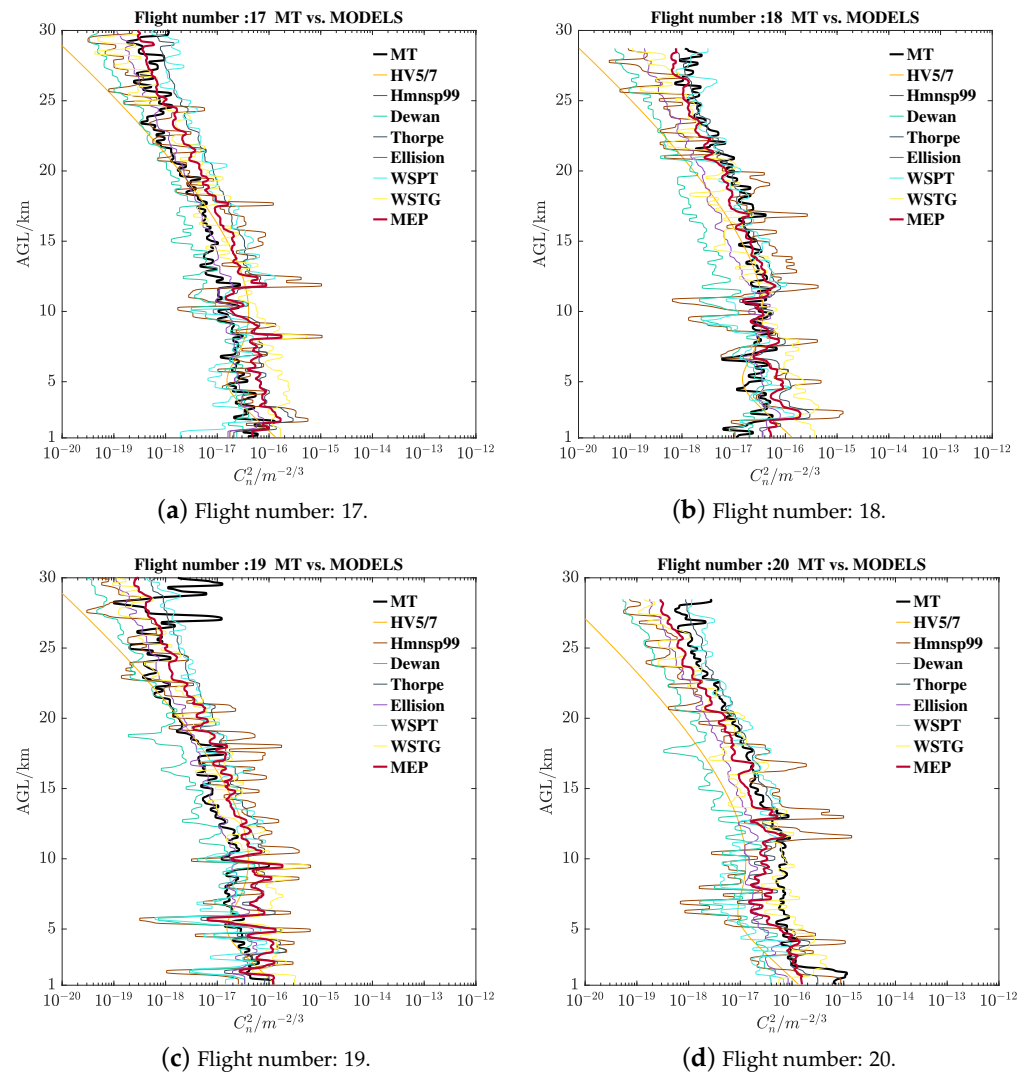


Figure A7. The refractive index structure parameter profiles of MT and estimations in NCACN: Figure A7 sub-figures (a–d) are flight numbers 17–20 in Table A2.

Appendix B.3. The Integrated Astronomical Parameters

Appendix B.3.1. ECACN Integrated Astronomical Parameters Details

The integrated astronomical parameters details calculated from radiosonde and model results in ECACN are included in Tables A3–A6.

Table A3. ECACN integrated astronomical parameters details (r_0 @ $\lambda = 550$ nm).

Parameter	Flight				Method					
	Number	MT	HV	H9	DN	TE	EN	WT	WG	ME
r_0/cm	1	6.45	15.41	5.95	19.31	4.25	4.08	10.48	5.92	5.30
	2	13.15	14.38	6.52	21.05	7.33	11.32	11.79	6.67	9.05
	3	21.22	16.91	4.80	22.64	8.72	15.68	12.40	6.98	10.10
	4	10.47	17.37	4.51	20.13	8.13	15.24	12.73	5.64	7.78
	5	5.63	18.97	6.43	20.46	7.50	13.76	10.94	6.34	9.34
	6	9.72	12.37	3.77	20.69	7.05	13.10	9.98	6.33	9.03
	7	10.63	12.53	4.51	20.72	7.28	14.47	11.04	6.64	7.56
	8	8.66	15.11	4.57	21.32	7.64	14.30	12.02	7.14	9.65
	9	15.61	19.53	5.68	21.35	7.69	14.93	16.86	6.92	9.21
	10	23.28	20.11	6.23	23.69	8.21	15.39	14.21	7.22	11.84

Table A3. Cont.

Parameter	Flight			Method						
	Number	MT	HV	H9	DN	TE	EN	WT	WG	ME
r_0/cm	11	18.69	19.12	7.52	21.14	8.01	14.69	12.23	7.03	9.71
	12	6.43	16.28	2.31	20.37	7.21	14.47	9.76	6.78	8.82
	13	9.19	15.40	4.08	22.02	7.38	14.27	9.58	6.82	8.06
	14	8.12	14.94	7.06	18.54	6.05	6.97	11.01	7.19	7.47
	15	12.90	13.44	6.36	19.82	7.41	14.82	12.43	6.70	8.66
	16	9.72	13.12	5.57	18.49	7.11	12.14	12.34	6.78	8.27
	Median	10.10	15.41	5.63	20.70	7.39	14.38	11.91	6.78	8.93
	Mean	11.87	15.94	5.37	20.73	7.31	13.10	11.86	6.69	8.74

Table A4. ECACN integrated astronomical parameters details ($\epsilon @ \lambda = 550 \text{ nm}$).

Parameter	Flight			Method						
	Number	MT	HV	H9	DN	TE	EN	WT	WG	ME
$\epsilon/''$	1	1.72	0.72	1.87	0.58	2.61	2.73	1.06	1.88	2.10
	2	0.85	0.77	1.71	0.53	1.52	0.98	0.94	1.67	1.23
	3	0.52	0.66	2.32	0.49	1.28	0.71	0.90	1.59	1.10
	4	1.06	0.64	2.47	0.55	1.37	0.73	0.87	1.97	1.43
	5	1.97	0.59	1.73	0.54	1.48	0.81	1.02	1.75	1.19
	6	1.14	0.90	2.95	0.54	1.58	0.85	1.11	1.76	1.23
	7	1.05	0.89	2.47	0.54	1.53	0.77	1.01	1.67	1.47
	8	1.28	0.74	2.43	0.52	1.46	0.78	0.92	1.56	1.15
	9	0.71	0.57	1.96	0.52	1.45	0.74	0.66	1.61	1.21
	10	0.48	0.55	1.79	0.47	1.35	0.72	0.78	1.54	0.94
	11	0.59	0.58	1.48	0.53	1.39	0.76	0.91	1.58	1.15
	12	1.73	0.68	4.81	0.55	1.54	0.77	1.14	1.64	1.26
	13	1.21	0.72	2.72	0.50	1.51	0.78	1.16	1.63	1.38
	14	1.37	0.74	1.57	0.60	1.84	1.59	1.01	1.55	1.49
	15	0.86	0.83	1.75	0.56	1.50	0.75	0.89	1.66	1.28
	16	1.14	0.85	1.99	0.60	1.56	0.92	0.90	1.64	1.34
	Median	1.10	0.72	1.98	0.54	1.50	0.77	0.93	1.64	1.25
	Mean	1.11	0.71	2.25	0.54	1.56	0.96	0.96	1.67	1.31

Table A5. ECACN integrated astronomical parameters details ($\theta_{AO} @ \lambda = 550 \text{ nm}$).

Parameter	Flight			Method						
	Number	MT	HV	H9	DN	TE	EN	WT	WG	ME
$\theta_{AO}/''$	1	0.33	1.23	0.69	1.69	0.57	0.99	0.84	0.57	0.69
	2	0.78	1.09	0.47	1.79	0.57	1.13	0.68	0.60	0.74
	3	2.01	1.47	0.31	1.89	0.62	1.20	0.70	0.58	0.77
	4	0.83	1.55	0.28	1.77	0.60	1.14	0.70	0.55	0.68
	5	0.52	1.91	0.42	1.74	0.59	1.02	0.64	0.55	0.73
	6	0.57	0.87	0.38	1.76	0.60	1.08	0.68	0.56	0.73
	7	0.85	0.88	0.31	1.67	0.60	1.18	0.74	0.55	0.54
	8	0.69	1.18	0.39	1.75	0.58	1.16	0.71	0.61	0.77
	9	1.36	2.07	0.46	1.77	0.58	1.16	1.00	0.61	0.75
	10	1.13	2.27	0.46	1.90	0.60	1.16	0.88	0.60	0.91
	11	1.10	1.95	0.47	1.77	0.59	1.12	0.76	0.60	0.73
	12	0.47	1.36	0.32	1.75	0.61	1.17	0.68	0.63	0.80
	13	0.46	1.23	0.47	1.86	0.59	1.14	0.67	0.63	0.66
	14	0.40	1.16	0.68	1.58	0.48	0.53	0.74	0.59	0.58
	15	0.65	0.98	0.61	1.73	0.58	1.15	0.83	0.62	0.71
	16	0.60	0.94	0.49	1.60	0.57	0.97	0.74	0.56	0.66
	Median	0.67	1.23	0.46	1.76	0.59	1.14	0.72	0.60	0.73
	Mean	0.80	1.38	0.45	1.75	0.58	1.08	0.75	0.59	0.72

Table A6. ECACN integrated astronomical parameters details (σ_I^2 @ $\lambda = 550$ nm).

Parameter	Flight		Method							
	Number	MT	HV	H9	DN	TE	EN	WT	WG	ME
σ_I^2	1	1.54	0.24	0.76	0.15	1.10	0.75	0.41	0.99	0.81
	2	0.40	0.28	1.04	0.13	0.80	0.30	0.49	0.87	0.54
	3	0.10	0.19	2.02	0.12	0.66	0.24	0.47	0.85	0.49
	4	0.44	0.17	2.44	0.14	0.73	0.26	0.46	1.03	0.67
	5	1.03	0.13	1.22	0.14	0.78	0.31	0.56	0.97	0.55
	6	0.63	0.40	1.95	0.14	0.82	0.31	0.57	0.95	0.58
	7	0.37	0.39	2.10	0.14	0.79	0.26	0.49	0.95	0.86
	8	0.61	0.25	1.61	0.14	0.78	0.26	0.49	0.82	0.51
	9	0.21	0.12	1.12	0.13	0.77	0.26	0.27	0.82	0.54
	10	0.18	0.11	1.08	0.12	0.72	0.25	0.34	0.82	0.38
	11	0.22	0.13	0.99	0.14	0.75	0.27	0.44	0.84	0.54
	12	1.01	0.21	3.18	0.14	0.78	0.26	0.57	0.82	0.52
	13	0.82	0.24	1.44	0.12	0.78	0.27	0.58	0.81	0.66
	14	1.02	0.26	0.72	0.17	1.18	1.05	0.49	0.84	0.85
	15	0.47	0.33	0.87	0.14	0.82	0.26	0.40	0.84	0.60
	16	0.63	0.35	1.16	0.16	0.84	0.37	0.46	0.92	0.67
Median		0.54	0.24	1.19	0.14	0.78	0.26	0.48	0.85	0.56
Mean		0.61	0.24	1.48	0.14	0.82	0.35	0.47	0.88	0.61

Appendix B.3.2. NCACN Integrated Astronomical Parameters Details

The integrated astronomical parameters details calculated from radiosonde and model results in NCACN are included in Tables A7–A10.

Table A7. NCACN integrated astronomical parameters details (r_0 @ $\lambda = 550$ nm).

Parameter	Flight		Method							
	Number	MT	HV	H9	DN	TE	EN	WT	WG	ME
r_0	1	2.95	17.18	3.74	19.16	6.84	8.21	12.00	5.21	7.12
	2	8.63	14.05	3.57	20.75	7.36	13.01	10.20	6.15	8.27
	3	9.04	14.56	3.85	21.19	7.50	14.53	10.75	6.64	8.16
	4	5.67	13.40	2.67	20.68	6.90	8.99	9.81	5.77	7.40
	5	4.93	12.47	3.96	17.86	7.79	15.88	8.42	6.19	8.03
	6	15.11	13.97	4.86	18.12	7.82	14.03	9.47	5.81	8.84
	7	7.19	15.95	5.82	18.41	7.76	16.78	10.38	6.20	5.66
	8	19.46	10.79	3.86	19.55	9.41	17.60	15.12	6.57	10.77
	9	9.86	10.72	4.16	20.76	8.94	15.73	10.18	6.40	10.73
	10	3.32	14.17	1.61	20.21	7.85	13.02	11.18	6.46	6.27
	11	13.17	11.67	3.99	19.27	7.60	14.78	9.66	6.57	7.11
	12	15.67	15.55	5.16	17.36	7.84	15.65	12.09	5.93	9.40
	13	13.35	18.65	6.17	20.62	8.16	16.50	14.61	6.91	9.29
	14	7.06	18.80	4.77	20.02	7.42	11.02	13.74	6.24	8.79
	15	10.77	21.23	4.92	21.43	8.19	12.19	12.68	6.11	9.73
	16	12.67	20.45	3.74	24.38	8.56	14.97	14.64	6.84	8.83
	17	16.23	13.34	6.61	20.65	8.50	16.84	12.93	6.82	9.93
	18	13.03	13.83	6.00	21.46	8.35	14.32	12.10	6.31	10.11
	19	15.06	13.40	6.60	20.38	8.86	16.90	13.65	7.10	9.62
	20	6.06	18.60	5.22	21.95	8.43	16.24	13.98	6.75	10.36
Median		10.31	14.11	4.46	20.50	7.84	14.88	12.04	6.36	8.83
Mean		10.46	15.14	4.56	20.21	8.00	14.36	11.88	6.35	8.72

Table A8. NCACN integrated astronomical parameters details (ϵ @ $\lambda = 550$ nm).

Parameter	Flight			Method						
	Number	MT	HV	H9	DN	TE	EN	WT	WG	ME
$\epsilon/''$	1	3.77	0.65	2.97	0.58	1.63	1.35	0.93	2.13	1.56
	2	1.29	0.79	3.12	0.54	1.51	0.85	1.09	1.81	1.34
	3	1.23	0.76	2.88	0.52	1.48	0.76	1.03	1.67	1.36
	4	1.96	0.83	4.17	0.54	1.61	1.24	1.13	1.93	1.50
	5	2.26	0.89	2.81	0.62	1.43	0.70	1.32	1.80	1.39
	6	0.74	0.80	2.29	0.61	1.42	0.79	1.17	1.91	1.26
	7	1.55	0.70	1.91	0.60	1.43	0.66	1.07	1.79	1.97
	8	0.57	1.03	2.88	0.57	1.18	0.63	0.74	1.69	1.03
	9	1.13	1.04	2.67	0.54	1.24	0.71	1.09	1.74	1.04
	10	3.35	0.78	6.92	0.55	1.42	0.85	0.99	1.72	1.77
	11	0.84	0.95	2.79	0.58	1.46	0.75	1.15	1.69	1.56
	12	0.71	0.71	2.16	0.64	1.42	0.71	0.92	1.87	1.18
	13	0.83	0.60	1.80	0.54	1.36	0.67	0.76	1.61	1.20
	14	1.57	0.59	2.33	0.56	1.50	1.01	0.81	1.78	1.26
	15	1.03	0.52	2.26	0.52	1.36	0.91	0.88	1.82	1.14
	16	0.88	0.54	2.97	0.46	1.30	0.74	0.76	1.62	1.26
	17	0.69	0.83	1.68	0.54	1.31	0.66	0.86	1.63	1.12
	18	0.85	0.80	1.85	0.52	1.33	0.78	0.92	1.76	1.10
	19	0.74	0.83	1.68	0.55	1.25	0.66	0.81	1.57	1.16
	20	1.83	0.60	2.13	0.51	1.32	0.68	0.80	1.65	1.07
Median	1.08	0.79	2.50	0.54	1.42	0.75	0.92	1.75	1.26	
Mean	1.39	0.76	2.71	0.55	1.40	0.81	0.96	1.76	1.31	

Table A9. NCACN integrated astronomical parameters details (θ_{AO} @ $\lambda = 550$ nm).

Parameter	Flight			Method						
	Number	MT	HV	H9	DN	TE	EN	WT	WG	ME
$\theta_{AO}/''$	1	0.49	1.52	0.35	1.82	0.62	0.97	0.91	0.54	0.72
	2	0.64	1.05	0.62	1.76	0.63	1.05	0.73	0.59	0.72
	3	0.61	1.11	0.36	1.98	0.66	1.23	0.69	0.63	0.71
	4	0.47	0.97	0.33	1.84	0.59	0.80	0.68	0.54	0.65
	5	0.41	0.88	0.24	1.86	0.63	1.30	0.55	0.57	0.67
	6	1.02	1.04	0.31	1.56	0.62	1.11	0.56	0.46	0.67
	7	0.35	1.31	0.56	1.63	0.63	1.38	0.68	0.58	0.53
	8	1.26	0.72	0.21	1.63	0.64	1.30	0.88	0.56	0.78
	9	0.51	0.71	0.26	1.71	0.65	1.19	0.63	0.57	0.75
	10	0.15	1.06	0.19	1.81	0.62	0.96	0.68	0.53	0.59
	11	0.97	0.80	0.29	1.86	0.64	1.16	0.65	0.61	0.59
	12	0.93	1.25	0.37	1.65	0.61	1.26	0.74	0.50	0.73
	13	1.02	1.83	0.39	1.96	0.61	1.28	0.78	0.65	0.77
	14	0.38	1.87	0.27	1.93	0.59	0.95	0.83	0.57	0.66
	15	0.51	2.75	0.75	1.80	0.63	0.92	0.79	0.58	0.76
	16	1.45	2.40	0.41	2.06	0.68	1.23	0.99	0.65	0.77
	17	1.29	0.97	0.45	1.77	0.63	1.31	0.66	0.59	0.77
	18	0.74	1.02	0.44	1.89	0.62	1.10	0.71	0.65	0.75
	19	1.06	0.97	0.43	1.70	0.62	1.28	0.77	0.59	0.73
	20	0.61	1.82	0.36	1.93	0.66	1.29	0.74	0.63	0.87
Median	0.63	1.06	0.36	1.82	0.63	1.21	0.72	0.58	0.72	
Mean	0.74	1.30	0.38	1.81	0.63	1.15	0.73	0.58	0.71	

Table A10. NCACN integrated astronomical parameters details (σ_I^2 @ $\lambda = 550$ nm).

Parameter	Flight Number	Method								
		MT	HV	H9	DN	TE	EN	WT	WG	ME
σ_I^2	1	2.28	0.18	1.94	0.14	0.80	0.50	0.36	1.16	0.69
	2	0.63	0.30	1.33	0.14	0.74	0.32	0.50	0.94	0.60
	3	0.69	0.27	1.90	0.12	0.69	0.25	0.52	0.82	0.62
	4	1.19	0.33	2.85	0.14	0.85	0.54	0.58	1.06	0.74
	5	1.66	0.39	2.96	0.15	0.72	0.22	0.79	0.99	0.68
	6	0.29	0.30	2.07	0.17	0.73	0.29	0.72	1.26	0.64
	7	1.38	0.22	0.99	0.16	0.73	0.20	0.53	0.97	1.10
	8	0.19	0.53	3.69	0.16	0.64	0.21	0.33	0.96	0.49
	9	0.79	0.54	2.83	0.14	0.65	0.25	0.63	0.93	0.50
	10	5.37	0.29	8.17	0.14	0.73	0.35	0.52	1.01	0.96
	11	0.36	0.45	2.42	0.14	0.74	0.26	0.62	0.88	0.85
	12	0.31	0.23	1.62	0.17	0.75	0.23	0.47	1.19	0.56
	13	0.32	0.14	1.40	0.13	0.72	0.22	0.40	0.80	0.54
	14	1.32	0.14	2.49	0.13	0.81	0.41	0.38	0.99	0.65
	15	0.74	0.09	0.77	0.13	0.68	0.39	0.41	0.96	0.51
	16	0.23	0.10	1.58	0.11	0.61	0.24	0.29	0.79	0.54
	17	0.22	0.34	1.18	0.14	0.69	0.21	0.51	0.91	0.52
	18	0.45	0.31	1.25	0.13	0.72	0.29	0.48	0.86	0.52
	19	0.27	0.33	1.26	0.15	0.69	0.22	0.41	0.86	0.57
	20	0.85	0.14	1.66	0.12	0.64	0.22	0.41	0.84	0.44
	Median	0.66	0.30	1.78	0.14	0.72	0.25	0.49	0.95	0.58
	Mean	0.98	0.28	2.22	0.14	0.72	0.29	0.49	0.96	0.64

References

1. Tatarskii, V.I. *Wave Propagation in a Turbulent Medium*; McGraw-Hill: New York, NY, USA, 1961.
2. Beckers, J.M. Adaptive optics for astronomy: Principles, performance, and applications. *Annu. Rev. Astron. Astrophys.* **1993**, *31*, 13–62. [[CrossRef](#)]
3. Coulman, C.E. Fundamental and applied aspects of astronomical seeing. *Annu. Rev. Astron. Astrophys.* **1985**, *23*, 19–57. [[CrossRef](#)]
4. Davies, R.; Kasper, M. Adaptive Optics for Astronomy. *Annu. Rev. Astron. Astrophys.* **2012**, *50*, 305–351. [[CrossRef](#)]
5. Fried, D.L. Limiting resolution looking down through the atmosphere. *J. Opt. Soc. Am.* **1966**, *56*, 1380–1385. [[CrossRef](#)]
6. Deng, L.; Yang, F.; Chen, X.; He, F.; Liu, Q.; Zhang, B.; Zhang, C.; Wang, K.; Liu, N.; et al. Lenghu on the Tibetan Plateau as an astronomical observing site. *Nature* **2021**, *596*, 353. [[CrossRef](#)] [[PubMed](#)]
7. Fugate, R.Q.; Fried, D.L.; Amer, G.A.; Boeke, B.R.; Browne, S.L.; Roberts, P.H.; Ruane, R.E.; Tyler, G.A.; Wopat, L.M. Measurement of atmospheric wave-front distortion using scattered-light from a laser guide-star. *Nature* **1991**, *353*, 144–146. [[CrossRef](#)]
8. Mahalov, A.; Moustakou, M. Characterization of atmospheric optical turbulence for laser propagation. *Laser Photonics Rev.* **2010**, *4*, 144–159. [[CrossRef](#)]
9. Roddier, F. V the Effects of Atmospheric Turbulence in Optical Astronomy. In *Progress in Optics*; Wolf, E., Ed.; Elsevier: Amsterdam, The Netherlands, 1981; Volume 19, pp. 281–376. [[CrossRef](#)]
10. Zhang, R.Z.; Hu, N.Z.; Zhou, H.B.; Zou, K.H.; Su, X.Z.; Zhou, Y.Y.; Song, H.Q.; Pang, K.; Song, H.; Minoofar, A.; et al. Turbulence-resilient pilot-assisted self-coherent free-space optical communications using automatic optoelectronic mixing of many modes. *Nat. Photonics* **2021**, *15*, 743–750. [[CrossRef](#)]
11. Zhu, Z.; Janasik, M.; Fyffe, A.; Hay, D.; Zhou, Y.; Kantor, B.; Winder, T.; Boyd, R.W.; Leuchs, G.; Shi, Z. Compensation-free high-dimensional free-space optical communication using turbulence-resilient vector beams. *Nat. Commun.* **2021**, *12*, 1666. [[CrossRef](#)]
12. Masciadri, E.; Vernin, J.; Bougeault, P. 3D mapping of optical turbulence using an atmospheric numerical model I. A useful tool for the ground-based astronomy. *Astron. Astrophys. Suppl. Ser.* **1999**, *137*, 185–202. [[CrossRef](#)]
13. Marks, R.D.; Vernin, J.; Azouit, M.; Briggs, J.W.; Burton, M.G.; Ashley, M.C.B.; Manigault, J.F. Antarctic site testing—Microthermal measurements of surface-layer seeing at the South Pole. *Astron. Astrophys. Suppl. Ser.* **1996**, *118*, 385–390. [[CrossRef](#)]
14. Qing, C.; Wu, X.; Li, X.; Luo, T.; Su, C.; Zhu, W. Mesoscale optical turbulence simulations above Tibetan Plateau: First attempt. *Opt. Express* **2020**, *28*, 4571–4586. [[CrossRef](#)] [[PubMed](#)]
15. Guryanov, A.E.; Kallistratova, M.A.; Kutyrev, A.S.; Petenko, I.V.; Shcheglov, P.V.; Tokovinin, A.A. The contribution of the lower atmospheric layers to the seeing at some mountain observatories. *Astron. Astrophys.* **1992**, *262*, 373–381.

16. Tokovinin, A.; Kornilov, V. Measuring turbulence profile from scintillations of single stars. In *Astronomical Site Evaluation in the Visible and Radio Range Workshop, IAU Technical Workshop, Proceedings of a Workshop Held at Cadi Ayyad University, Marrakech, Morocco, 13–17 November 2000*; Astronomical Society of the Pacific Conference Series; Astronomical Soc Pacific: San Francisco, CA, USA, 2002; Volume 266, pp. 104–112.
17. Osborn, J.; Wilson, R.; Butterley, T.; Shepherd, H.; Sarazin, M. Profiling the surface layer of optical turbulence with SLODAR. *Mon. Not. R. Astron. Soc.* **2010**, *406*, 1405–1408. [[CrossRef](#)]
18. Wang, Z.Y.; Zhang, L.Q.; Kong, L.; Bao, H.; Guo, Y.M.; Rao, X.J.; Zhong, L.B.; Zhu, L.; Rao, C.H. A modified S-DIMM plus: Applying additional height grids for characterizing daytime seeing profiles. *Mon. Not. R. Astron. Soc.* **2018**, *478*, 1459–1467. [[CrossRef](#)]
19. Kovadlo, P.G.; Shikhovtsev, A.Y.; Kopylov, E.A.; Kiselev, A.V.; Russkikh, I.V. Study of the Optical Atmospheric Distortions using Wavefront Sensor Data. *Russ. Phys. J.* **2021**, *63*, 1952–1958. [[CrossRef](#)]
20. Deng, J.; Song, T.; Liu, Y. Development Overview of Daytime Atmospheric Optical Turbulence Profile Detection Technology. *Prog. Astron.* **2022**, *40*, 345–363.
21. Basu, S. A simple approach for estimating the refractive index structure parameter (C_n^2) profile in the atmosphere. *Opt. Lett.* **2015**, *40*, 4130–4133. [[CrossRef](#)]
22. Hufnagel, R.E.; Stanley, N.R. Modulation Transfer Function Associated with Image Transmission through Turbulent Media. *J. Opt. Soc. Am.* **1964**, *54*, 52–61. [[CrossRef](#)]
23. Barletti, R.; Ceppatelli, G.; Paternò, L.; Righini, A.; Speroni, N. Mean vertical profile of atmospheric turbulence relevant for astronomical seeing. *J. Opt. Soc. Am.* **1976**, *66*, 1380–1383. [[CrossRef](#)]
24. Ruggiero, H.; DeBenedictis, D.A. Forecasting optical turbulence from mesoscale numerical weather prediction models. In Proceedings of the DoD High Performance Modernization Program Users Group Conference, Vicksburg, MS, USA, June 2002.
25. Dewan, E.M.; Grossbard, N. The inertial range “outer scale” and optical turbulence. *Environ. Fluid Mech.* **2007**, *7*, 383–396. [[CrossRef](#)]
26. Thorpe, S.A. *The Turbulent Ocean*; Cambridge University Press: Cambridge, UK, 2005; Volume 9780521835435. [[CrossRef](#)]
27. Ellison, T.H. Turbulent transport of heat and momentum from an infinite rough plane. *J. Fluid Mech.* **1957**, *2*, 456–466. [[CrossRef](#)]
28. Wu, S.; Su, C.D.; Wu, X.Q.; Luo, T.; Li, X.B. A Simple Method to Estimate the Refractive Index Structure Parameter (C_n^2) in the Atmosphere. *Publ. Astron. Soc. Pac.* **2020**, *132*, 11. [[CrossRef](#)]
29. Wu, S.; Wu, X.Q.; Su, C.D.; Yang, Q.K.; Xu, J.Y.; Luo, T.; Huang, C.; Qing, C. Reliable model to estimate the profile of the refractive index structure parameter (C_n^2) and integrated astroclimatic parameters in the atmosphere. *Opt. Express* **2021**, *29*, 12454–12470. [[CrossRef](#)] [[PubMed](#)]
30. Xu, M.M.; Shao, S.Y.; Weng, N.Q.; Liu, Q. Analysis of the Optical Turbulence Model Using Meteorological Data. *Remote Sens.* **2022**, *14*, 3085. [[CrossRef](#)]
31. Vanzandt, T.E.; Gage, K.S.; Warnock, J.M. Statistical-model for probability of turbulence and calculation of vertical profiles of turbulence parameters. *Bull. Am. Meteorol. Soc.* **1978**, *59*, 1230.
32. Trinquet, H.; Vernin, J. A statistical model to forecast the profile of the index structure constant C_N^2 . *Environ. Fluid Mech.* **2007**, *7*, 397–407. [[CrossRef](#)]
33. Bi, C.C.; Qing, C.; Wu, P.F.; Jin, X.M.; Liu, Q.; Qian, X.M.; Zhu, W.Y.; Weng, N.Q. Optical Turbulence Profile in Marine Environment with Artificial Neural Network Model. *Remote Sens.* **2022**, *14*, 2267. [[CrossRef](#)]
34. Bolbasova, L.A.; Andrakhanov, A.A.; Shikhovtsev, A.Y. The application of machine learning to predictions of optical turbulence in the surface layer at Baikal Astrophysical Observatory. *Mon. Not. R. Astron. Soc.* **2021**, *504*, 6008–6017. [[CrossRef](#)]
35. Wang, Y.; Basu, S. Using an artificial neural network approach to estimate surface-layer optical turbulence at Mauna Loa, Hawaii. *Opt. Lett.* **2016**, *41*, 2334–2337. [[CrossRef](#)]
36. Gladstone, J.H.; Dale, T.P. Researches on the Refraction, Dispersion, and Sensitiveness of Liquids. *Philos. Trans. R. Soc. Lond.* **1863**, *153*, 317–343.
37. Chen, X.W.; Li, X.B.; Sun, G.; Liu, Q.; Zhu, W.Y.; Weng, N.Q. Effects of intermittency and stratification on the evaluation of optical propagation. *Chin. Opt. Lett.* **2017**, *15*, 5. [[CrossRef](#)]
38. Taylor, K.E. Summarizing multiple aspects of model performance in a single diagram. *J. Geophys. Res.-Atmos.* **2001**, *106*, 7183–7192. [[CrossRef](#)]
39. Haslebacher, C.; Demory, M.E.; Demory, B.O.; Sarazin, M.; Vidale, P.L. Impact of climate change on site characteristics of eight major astronomical observatories using high-resolution global climate projections until 2050 Projected increase in temperature and humidity leads to poorer astronomical observing conditions. *Astron. Astrophys.* **2022**, *665*, 53. [[CrossRef](#)]
40. Yang, Q.K.; Wu, X.Q.; Wang, Z.Y.; Hu, X.D.; Guo, Y.M.; Qing, C. Simulating the night-time astronomical seeing at Dome A using Polar WRF. *Mon. Not. R. Astron. Soc.* **2022**, *515*, 1788–1794. [[CrossRef](#)]

Disclaimer/Publisher’s Note: The statements, opinions and data contained in all publications are solely those of the individual author(s) and contributor(s) and not of MDPI and/or the editor(s). MDPI and/or the editor(s) disclaim responsibility for any injury to people or property resulting from any ideas, methods, instructions or products referred to in the content.